Supplementary Material

Holocene glacier readvances on the Fildes Peninsula, King George Island (Isla 25 de Mayo), NW Antarctic Peninsula

Pablo Heredia Barión[1,2,3], Stephen J. Roberts[4*], Cornelia Spiegel[2], Steven A. Binnie[5], Lukas Wacker[6], Joanna Davies[7], Imogen Gabriel[8], Vivienne J. Jones[7], Simon Blockley[8], Emma J. Pearson[9], Louise Foster[4,9], Sarah J. Davies[10], Thomas P. Roland[11], Emma P. Hocking[12], Michael J. Bentley[13], Dominic A. Hodgson[4,13], Chris L. Hayward[14], Robert D. McCulloch[14,15], Jorge A. Strelin[3, 16], Gerhard Kuhn[1,2]

[1]Alfred-Wegener-Institut Helmholtz-Zentrum für Polar- und Meeresforschung, Geosciences Division, Am Alten Hafen 26, 27568 Bremerhaven, Germany.
[2]University of Bremen, Department of Geosciences, Klagenfurter Str. 2–4, 28359 Bremen, Germany.
[3]Centro de Investigaciones en Ciencias de la Tierra (CONICET-UNC), Vélez Sársfield 1611, X5016GCA, Córdoba, Argentina.
[4]British Antarctic Survey (BAS), Natural Environmental Research Council (NERC), High Cross, Madingley Road, Cambridge CB3 0ET, UK.
[5]Institute for Geology und Mineralogy, University of Cologne, Zuelpicher Str. 49b, Cologne D-50674, Germany.
[6]ETH Zürich, Laboratory of Ion Beam Physics, Schafmattstrasse 20, CH-8093 Zürich, Switzerland.
[7]ECRC Dept. of Geography, University College London, North West Wing, Gower St, London WC1E 6BT, UK.
[8]Dept. of Geography, Royal Holloway, University of London, Egham, Surrey, TW20 OEX, UK.
[9]School of Geography, Politics and Sociology, Newcastle University, Newcastle-upon-Tyne, NE1 7RU, UK.
[10]Aberystwyth University, Department of Geography and Earth Sciences, Aberystwyth, SY23 3DB, UK.
[11]Department of Geography, University of Exeter, Exeter EX4 4RJ, UK.
[12]Department of Geography, Northumbria University, Ellison Building, Newcastle-upon-Tyne NE1 8ST, UK.
[13]Department of Geography, Durham University, Durham DH1 3LE, UK.
[14]School of Geosciences, Grant Institute, University of Edinburgh, The King's Buildings, Edinburgh EH9 3FE.
[15]Centro de Investigación en Ecosistemas de la Patagonia, Coyhaique, Aysén, Chile.
[16]Instituto Antártico Argentino, Convenio MREC - Universidad Nacional de Córdoba, Vélez Sársfield 1611, X5016GCA, Córdoba, Argentina.

*Corresponding author: Stephen J. Roberts (sjro@bas.ac.uk)

1. Sample processing for ^{10}Be exposure dating

Purified quartz separates were prepared from the rock samples at Bremen University cosmogenic nuclide laboratory. We used standard physical rock preparation: a jaw crusher, sieves (125–1000 µm) and Frantz magnetic separation (up to 1.5 A). Unwanted phases such as feldspar and carbonates were removed from the non-magnetic fraction by chemical purification using 30% HCl + 0.03% H_2O_2 leaching. The resulting, almost pure, quartz and feldspar sample was further cleaned of meteoric beryllium by 3 steps of weak 2% HNO_3 + 2% HF leaching. Sample mass was weighed before and after to track mass lost during processing.

Separation of beryllium from the quartz separates was carried out at the Institute for Geology und Mineralogy, University of Cologne, Germany. Quartz purity was determined prior to dissolution by ICP-OES. Samples were then spiked with ~300 micrograms of commercially available beryllium (Be) carrier (Scharlab, 1000 microgram/l Beryllium ICP standard solution, batch number 14569501). After digestion in HF acid, remaining insoluble fluoride salts were heated several times in the presence of aqua regia and an aliquot of the sample was taken for an ICP-OES measurement before the sample underwent column separation using the single-step column procedure (Binnie et al., 2015). The separated $Be(OH)_2$ was co-precipitated alongside Ag (Stone et al., 2004) with a respective mass ratio of around 1:5, before being pressed into Cu targets for measurement on Cologne AMS, Institute of Nuclear Physics, University of Cologne (Dewald et al., 2013).

^{10}Be/^{9}Be AMS measurements were normalised to the standards of Nishiizumi using the nominal values (Nishiizumi et al., 2007). A blank was prepared in tandem with the samples and ^{10}Be concentrations are reported following subtraction of the ^{10}Be atoms measured in the blank. Though sample concentrations are relatively low, the maximum blank subtraction was <6%. Analytical uncertainties for the ^{10}Be concentrations were derived by summing in quadrature the uncertainty in the mass of Be added during sample processing (estimated to be 1% at 1 sigma) and the AMS measurement uncertainties of both the samples and blank.

2. Kiteschsee Lake

Located at ~15 m above present sea level (m a.s.l.), Kiteschsee Lake is one of the largest seasonally ice-free lakes on the northern Antarctic Peninsula, with dimensions of ~430 m x 220 m and a surface area of 0.09 km^2. During the Austral winter, the lake is covered by 50 cm of lake-ice, which usually melts by late Austral spring/early summer (November-December) (Martinez-Macchiavello et al., 1996; Barnard et al., 2014).

2.1 Methods

Multi-proxy analysis of a new ~77 cm long and c. 7.5 ka Kiteschsee Lake sediment record was used to reconstruct Holocene environmental change in the mid-outer area of Fildes Peninsula.

Lithology and Geochemistry: The Kiteschsee Lake composite record consists of two overlapping cores, aligned using magnetic susceptibility and XRF core scanning (XRF-CS) data (Figure S1, S2). Stratigraphic diagrams of %LOI (Loss-on-ignition of dry sediment at 550 °C for 4 hours), wet-sediment XRF-CS geochemistry and grain size were created in C2 v.1.7.7 and Sigmaplot, and data analysed using the R packages Vegan and Rioja (Juggins, 2007; Juggins, 2022; Oksanen, 2014); Systat Software Inc.).

ITRAX^{TM} XRF-CS was performed contiguously at 0.02 cm (200 µm) intervals using an Mo-tube (45 kV, 50 mA, 500 µm), with X-radiographs (45 kV, 35 mA, 200 ms) taken as part of the same run following established procedures (Davies et al., 2015; Roberts et al., 2017). Machine and sample calibration were undertaken at the start and end of each analytical phase using a synthetic glass standard and XRF fused glass discs made from bulk sediment samples from the nearby Yanou Lake

and Ardley Lake records. Raw count per second (cps) data were analysed using the Cox Analytical Q-spec software. To account for downcore variations in count rate, density, water and organic content, XRF-CS data are presented as relative changes in percentages of the Total Scatter Normalised ratio sum (%TSN), which is equivalent to the %cps sum (Roberts et al., 2022), and as natural log ratios and centred log ratios (clr). Log ratios can produce similar downcore patterns to quantitative Wavelength Dispersive Spectroscopy (WDS), dry subsample XRF analysis (Kylander et al., 2011; Davies et al., 2015; Roberts et al., 2017; Saunders et al., 2018; Dunlea et al., 2020). Data were filtered to remove a small number (<1%) of downcore spectra with kcps less than mean minus two-SD kcps, caused mainly by small gaps in the core, and MSE values greater than mean plus four-SD, which represents a poor fit of the measured to theoretical energy spectra. Key 'measurable' elements were determined using autocorrelation and significant zones and their boundary positions were defined using constrained cluster analysis (CONISS) with broken stick analysis applied to square-root-transformed %TSN values of key elements in R packages Vegan and Rioja (Juggins, 2022; Oksanen, 2014).

Whole core gamma (bulk) wet density, magnetic susceptibility (Bartington Instruments MS2E point sensor, 10 second count time; true χ_{vol} data), and P-wave amplitude and velocity were measured at 5 mm intervals using GEOTEK multi-sensor core logger (MSCL) and following standard calibration procedures.

Sediment grain size was measured using a Malvern laser particle counter that detects particles between 0.01-2,000 µm. Samples were organic-free (post Loss-on Ignition, LOI) and carbonate-free (5% HCl pre-treatment). Calgon was added to the sample to reduce aggregation before being diluted. Grain size data was analysed using GRADISTAT (Blott and Pye, 2001). As diatom abundance was high throughout the core, we examined the impact of diatoms on grain size distributions using four sediment samples from 6 cm, 13 cm, 20 cm, and 33.5 cm, using sodium hydroxide for dissolving biogenic opal. Results showed minimal difference in grain size distribution, insufficient to undertake the process for all samples.

The positions of several prominent visible tephra layers (T_n) that were apparent in XRF-CS data as elevated Ti, Ca, K, and incoherent/coherent scattering ratio minima, were confirmed using manual shard counting following methods in Blockley et al. (2005). Shard-specific geochemical analysis of shards from two key layers at 33 cm and 58 cm depth is described in a separate section below.

C-14 dating: Radiocarbon dating of Antarctic Lake sediments from high latitudes is often problematic due to prolonged ice cover, low terrestrial and aquatic biological production, slow rates of organic matter (OM) decomposition and the presence of old-carbon reservoirs in sediment, ice, and water. Bulk glaciolacustrine sediments have produced 'reliable' ages in some lake records from Fildes Peninsula, often overlapping with paired macrofossil ages and tephra-based chronologies from well-dated terrestrial and marine records (Watcham et al., 2011; Roberts et al., 2017). Dried bulk sediment and aquatic moss samples were radiocarbon dated by Beta Analytic, Miami, using standard procedures outlined in the Supplementary Material of Roberts et al. (2017).

Age-depth modelling: An age depth model for the Kiteschsee Lake record was constructed using new radiocarbon ages and age data for the most prominent visible tephra deposits. The latter were obtained by comparison to the most prominent tephra layers, T1–T5, in the Yanou Lake record, which are well constrained by radiocarbon dating of aquatic moss. The ages of the T1-T5 layers were also compared to the most prominent visible tephra layers in lake records from Fildes Peninsula (Ardley Lake, Belen Lake, Long Lake, Gaoshan Lake), and elsewhere on King George Island, the South Shetland Islands, and the James Ross ice (JRI) core record (Björck et al., 1993; Mulvaney et al., 2012; Roberts et al., 2017, Oliva et al., 2019) (Table S1; Figure S7).

Age-depth modelling was undertaken using BACON v.2.5 (Bayesian) age-depth modelling software using uncalibrated conventional radiocarbon age data as inputs and the SHCal20 calibration curve (Blaauw, 2010; Blaauw and Christen, 2011; Trachsel and Telford, 2016; Hogg et al., 2020). Prior settings for the initial [and final] KITE age-depth model runs were: acc.shape = 1.5, acc.mean = 100 [50] a cm^{-1}, mem.strength = 20, mem.mean = 0.4, segment thickness = 3 cm. Age-depth models were built as age = f(depth) + error and reversed with the rotate.axes function. All 'as measured' (uncalibrated) conventional radiocarbon age data were included in an initial model run, KITE-M1 (Figure S4A), without reservoir corrections or hiatuses and refined over further model runs to KITE-M4 (Figure S4B).

To obtain age estimates for the most prominent visible tephra deposits, tephra correlation age constraints were excluded from the initial model run (Figure S2, S7). Tephra deposits thicker than 1 cm at 10.5–12.1 cm, 32–34.3 cm and 58–63.5 cm depth were defined by CONISS analysis of the ITRAX 2 mm dataset and excluded from the final age-depth model with the slump function. We also investigated the effect of varying the mean accumulation rate setting using acc. mean settings of 10, 20 and 50 a cm^{-1} and 100 a cm^{-1} and the effect of using different segment thickness settings. For the final age model, an acc. mean of 50 a cm^{-1} and a segment thickness of 3 cm produced the best fit to measured data and the smallest errors.

Diatom analysis: Since the Early Holocene isolation history of Kiteschsee Lake is well-established (Mäusbacher et al., 1989), we undertook high-resolution analysis of diatoms that were well-preserved in the Late Holocene section of the new composite ~77 cm long, c. 7.5 ka record. To assess limnological and ecological responses to deglaciation and reconstruct downcore changes in chlorophyll-a associated with glacier readvance and climate, we applied a diatom-based transfer function. Multivariate Principal Component Analysis (PCA) was undertaken on log$_{10}$ transformed diatom data to explore the trends and assemblage changes in diatom communities and diatom response to changes in lake sediment geochemistry. A square root function was also applied to percentage count data to reduce the score bias of the most abundant species which could mask the influence of less abundant species.

Detrended Correspondence Analysis (DCA) was used to identify whether unimodal or linear models were most suitable for further analysis (ter Braak and Smilauer, 2002). DCA showed that the gradient length is short (<2 standard deviation units), meaning linear methods (PCA, RDA) were more appropriate. Relationships between the diatom assemblages and environmental variables were explored further using RDA (Figure S10). The significance ($p < 0.05$) of each environmental variable was assessed with forward selection using an unrestricted Monte Carlo Permutation Test. Diatom compositional turnover (β-diversity) was estimated using Detrended Canonical Correspondence Analysis (DCCA) applied to the most abundant diatoms (>2%), with log transformation prior to statistical analysis using CANOCO 5.0 for Windows (Jones and Juggins, 1995; ter Braak and Smilauer, 2002). To infer changes in chlorophyll-a, we used the diatom-based chlorophyll-a modern training set from 61 Antarctic Peninsula lakes (Jones and Juggins, 1995). Diatom-based transfer functions were created in C2 (Juggins, 2007) using simple weighted averaging (WA) and weighted averaging partial least squares (WA-PLS) algorithms. The WA-Inverse transfer function was chosen to reconstruct chlorophyll-a because RMSE and average bias were low, and a strong correlation existed between measured and diatom-inferred chlorophyll-a.

GDGT analysis: Glycerol dialkyl glycerol tetraether (GDGT) analysis of freshwater-brackish sediments from Yanou Lake dating to c. 6 ka was used to reconstruct mean summer air temperature (MSAT) and MSAT anomaly profiles (relative to the pre-industrial mean 1–0.25 cal. ka BP; RMSE = 2.45 °C; Pearson et al., 2011; Foster et al., 2016; Roberts et al., 2017). The published GDGT palaeotemperature reconstructions for Yanou Lake in Roberts et al. (2017) overestimated MSAT for data older than 2000 years due to a lack of data at the upper end of the Foster et al. (2016) Antarctic calibration dataset. Therefore, we constructed a new MSAT anomaly profile by combining GDGT-

MSAT data from the global (Pearson et al., 2011) and Antarctic (Foster et al., 2016) GDGT calibration datasets and applied a new regression model based on the same compounds used in both (Juggins pers. comm). This produced a revised mean MSAT anomaly of 0.06±1.50 °C for the last 6,000 years of the Yanou Lake record, which is of a similar magnitude to the James Ross Island ice core mean annual temperature anomaly of 0.01±0.35 °C in the same period.

2.2 Results and Interpretations

Age-depth modelling & Tephra ages: Initial model run ages for sediment below tephra layers at 77-72 cm depth of 7,590–7,000 cal. a BP (weighted mean age range) overlap with the weighted mean age ± 2σ of the T7 tephra layer of 7,430±140 cal. a BP in the freshwater sediments of Ardley Lake (at a similar altitude (~15 m amsl) to Kiteschsee Lake). The T7 layer in the Yanou Lake record, at c. 11 m a.s.l., also has a similar age but it was deposited into shallow marine sediments.

The broad tephra peak between 62–56 cm in the Kiteschsee Lake record had a modelled weighted mean age range of 5,600–5,230 cal. a BP in the first model run, consistent with: 1) the 5,570±120–4,760±160 cal. a BP weighted mean ± 2σ age range of freshwater aquatic mosses dated below and above the T5 tephra deposit in the Yanou Lake record (Figure S2, S4); 2) the c. 5.5–4.5 ka age for the largest airfall tephra deposit in five other lakes on Fildes Peninsula (Watcham et al., 2011; Roberts et al., 2017); 3) independently-dated airfall ash deposits in lake, marine and ice core records elsewhere on the South Shetland Islands and the northern Antarctic Peninsula (Björck et al., 1991a, b, c; Willmott et al., 2006; Mulvaney et al., 2012; Antoniades et al., 2018; Oliva et al., 2019).

Initial model runs produced a mean ± 95% confidence interval (CI) age of $5,180 \frac{+1090}{-1050}$ cal. a BP for the fine rhyolitic cryptotephra layer at 58 cm depth (KITE_58). This deposit occurs in a prominent tephra deposit between 62–56 cm in the Kiteschsee Lake record and this age overlaps with the age of most prominent tephra deposit, T5, in the Yanou Lake record (Figure 4). The T5 layer in Yanou Lake is constrained by ages from aquatic moss immediately below (Y5a: 5,570±120 cal. a BP) and above (Y5b: 4,760±160 cal. a BP) a thick solifluncted reworked 'slump' deposit (ages recalibrated in SHCal20 using data in Roberts et al. (2017)). A prominent tephra layer at 45–40 cm depth had an initial model run age of 3,410±300 cal. a BP, overlapping with the 3,550±100 cal. a BP age of the T3a layer in the Yanou Lake record. This was followed by a tephra peak at 33 cm depth, aligned with T2 in the Yanou Lake record and two closely-spaced Late Holocene visible tephra deposits at 12–13 cm and 7.5–8 cm depth in the Kiteschsee Lake record, aligned with T1a and T1b in the Yanou Lake record (Figure 4, S2; Table S1).

We included the following aquatic moss radiocarbon ages associated with the three most prominent visible tephra deposits from the nearby Yanou Lake record as additional anchor points in the final age depth model, KITE-M4 (Figure S4B): 1) T1a, at 5.5 cm depth in the Yanou Lake record which has a radiocarbon age of 910±40 [14]C a BP (720±180 cal. a BP) applied at 12 cm depth in the Kiteschsee Lake record, below the most prominent ash layer in the top 15 cm of; 2) T3a, the first of three closely-spaced tephra deposits, at 20 cm depth in the Yanou Lake record of 3,370±30 [14]C a BP (3,630±170 cal. a BP), applied at 42.5 cm in Kiteschsee Lake; 3) Two radiocarbon ages from moss deposits below (190 cm depth) and above (58 cm depth) the most prominent T5 tephra deposit in the Yanou Lake record of 4,890±40 and 4,270±40 [14]C a BP (5,570±120 and 3,550±100 cal. a BP) applied before and after the most prominent tephra deposits in Kiteschsee Lake at 62–56 cm depth (Table S1). A final (tuned) modelled mean ± 95% CI age of $5,550 \frac{+150}{-200}$ cal. a BP was obtained for the KITE_58 layer in the Kiteschsee Lake record (Figure 4B, Table S1).

Lake reservoir offsets: Bulk sediment δ^{13}C values of −18.4 ppm from 5–6 cm depth are more aligned with δ^{13}C values of −18.0 and −17.7 ppm in the lower half of the core, meaning bulk sediments above 9 cm and below 25 cm are not as influenced by reworked old carbon most likely responsible for the

large bulk sediment age offset in Unit 7 at 20–21 cm depth (δ^{13}C -32.6 ppm; −23.9 ppm at 9–10 cm in Unit 9) (Table 2). A 700±100 ^{14}C year reservoir age was applied to bulk sediment radiocarbon ages from Units 7–9. This was calculated as the average difference between the modelled ages of the tephra layers T1a and T1b in the Yanou Lake record and uncorrected radiocarbon ages for closely-spaced tephra peaks in the Kiteschsee Lake record at 9–10 cm (T1a offset=710±130 years) and 7–8 cm (T1b offset=690±70 years) (Figure 4B, S2; Table S1). The similarity of the T2, T3 and T5 ages between the Kiteschsee and Yanou lake records in initial and final age-depth model runs also suggests no lake reservoir effect exists below 25 cm depth. The 95% CI age range of 2,100–1,460 cal. a BP (1,690 $^{+410}_{-230}$ cal. a BP, mean ±95% CI age range) for the second most prominent tephra layer at 33 cm depth (K33) in the Kiteschsee Lake record overlaps with the age of the T2 layer in the Yanou Lake record (95% CI age range of 2,390–1,850 cal. a BP) (Roberts et al., 2017) and the T2 layer in lakes from Barton Peninsula (2,370±100 cal. a BP) (Oliva et al., 2019).

Hiatus: Alpha spectrometry Lead-210 (^{210}Pb) dating of sediments between 6 and 11 cm depth revealed extremely low ^{210}Pb activity levels <10 Bq kg^{-1}, equivalent to background values, implying an age of >150–200 years (Figure S6); hence, a hiatus of 200 years was included in the age-depth model at 5 cm depth between the modern aquatic moss age at 4.5–5 cm depth (Unit 10) and the bulk sediment reservoir corrected age (±2σ) at 5–6 cm in Unit 9 of 560±180 cal. a BP (Figure 4, Table 2; Figure S6; Figure S7). Living aquatic moss at 0–1 cm and 4-5 cm depth returned similar post-bomb ages of 1956/57±1 CE (-7/-6±1 cal. a BP) (Figure 4; Table 2, 3).

Diatom results and interpretations:

Using constrained cluster analysis, we divided the diatom record into five zones, interpreted as follows:

Diatom Zone 1 (47-41.5 cm; 3,980–3,280 cal. a BP): This zone is initially dominated by a mix of both motile and attached forms (e.g., *C. pseudoscutiformis, S. pinnata*) plus some species associated with aquatic mosses; with increasing *P. abundans*.

Diatom Zone 2 (41.5-33.5 cm, 3,280–1,730 cal. a BP): Although Zones 1–2 have low diatom accumulation rates, Zone 2 exhibits decreasing β-diversity.

Diatom Zone 3 (33.5–22 cm; 1,730–1,300 cal. a BP): Species turnover in this zone was higher and the lake remained nutrient-poor, with a low diatom accumulation rate. Zone 3 is distinguished by the high abundance of *D. balfauriana* an aerophilic species which grows in wet catchment environments or in 'drier' littoral habitats of the lake (Oppenheim and Ellis-Evans, 1989; Spaulding et al., 1997). At the base of Zone 3, the dominance of the aerophilic diatom, *D. balfouriana*, *Gomphonema species 2* and *A. exigua* (commonly found on wet soils and terrestrial mosses), is indicative of warmer and/or wetter catchment conditions (Spaulding et al., 2010; Van de Vijver et al., 2012).

β-diversity (DCCA axis 1) is highest in this zone, probably driven by the appearance of new species (e.g., *C. subpampeana* and *P. divergens var linearis*) (Figure 4, S9). While inferred chlorophyll-a values could reflect cooler and less productive conditions, colonisation from new benthic species suggests the establishment of diatom communities more often associated with warmer climates (Björck et al., 1993; Björck et al., 1996). Reconstructing an unequivocal climate signal from diatom assemblages in lake sediments is complex because diatoms usually respond to changes in water chemistry and turbidity rather than temperature directly (Jones and Juggins, 1995). Nevertheless, deglaciation and warming can have an impact on catchment processes, affecting nutrient supply, diatom compositional turnover (β-diversity) and turbidity within lakes (Spaulding et al., 2010). Late 20th century warming has increased primary productivity and β-diversity in the Marguerite Bay region, Antarctica (Hodgson et al., 2013) and in Arctic lakes (Hobbs et al., 2010).

Diatom Zone 4 (22–13 cm; 1,300–840 cal. a BP): The assemblage in these zones is dominated by *S. pinnata*, a species which is tolerant of turbid conditions, and *P. abundans*, an attached form commonly found in dilute Antarctic lakes with low conductivity (Van de Vijver, 2008; Van de Vijver et al., 2010). Inferred chlorophyll-a is low (less than 10 µgl^{-1}) throughout this zone, indicating that very oligotrophic conditions persisted through the Late Holocene. Whilst the most abundant fossil diatom species in Kiteschsee Lake are well represented in the chlorophyll-a training set (89.4%), some key species such as *D. balfouriana, C. pseudoscutiformis* and *A. muelleri* are absent, affecting the reliability of the reconstruction.

In the McMurdo Dry Valleys, colder temperatures reduce diatom species diversity, with a limited number of species becoming dominant (Esposito et al., 2008). A substantial decline occurred in β-diversity in Kiteschsee Lake in Zone 4 (Figure 4, S9) and in *D. balfouriana* and *Gomphonema sp. 2* between Zones 3 and 4 and after c. 1.3 cal. ka BP, where they were almost completely absent. Interestingly, the most significant changepoint and decline in the Yanou Lake reconstructed temperature records occurred at c. 1.3 cal. ka BP (Figure S11). The coeval decline in *A. exigua*, an epiphytic species found on aquatic and terrestrial mosses indicative of humid soil (Martinez-Macchiavello et al., 1996; Van de Vijver and Beyens, 1997), could reflect a reduction in suitable littoral or terrestrial habitats in colder conditions (Sterken et al., 2008). Together, these species have been used as indicators of low productivity and cooler 'Neoglacial' conditions in similar environments along the Antarctic Peninsula (Björck et al., 1991a, 1993, 1996; Gibson and Zale, 2006).

The attached benthic species *S. pinnata* increased at 20–21 cm depth, at c. 1.1 cal. ka BP, in the glaciolacustrine lithofacies Unit 8. This species thrives in turbid and poor-quality water, absorbing nutrients better than its competitors due to their higher surface area to volume ratio (Reynolds, 1984; Michel et al., 2006). It is often found in recently deglaciated areas and colonizing harsh, light-poor environments (Haworth, 1976). In Kiteschsee Lake, it indicates particularly nutrient-poor and increasingly more turbid and colder 'Neoglacial' conditions. This shift in sedimentology and species assemblage also coincides with a decline in motile benthic species (e.g., *H. hungarica, P. divergens var linearis, C. subpampeana*) that favour calmer lake conditions.

Diatom Zone 5 (13–6 cm; 800–480 cal. a BP). The broad trends initiated in Zone 4 continue in Zone 5, and the transition is characterised by another significant changepoint shift to lower temperatures in the Yanou Lake record at c. 0.8 cal. ka BP (Figure S11). Lower β-diversity in this zone reflects a persistently turbid lake environment and this depositional style remains until a dramatic shift to an aquatic moss (*Drepanocladus longifolius (Mitt. Paris)* sp.) dominated environment in the mid-late C20th, which we associate with the late C20th Recent Rapid Warming (RRR) on the AP (Bentley et al., 2009) (Figure S12).

Airfall and reworked tephra deposition can also impact diatom communities. Tephra can lead to a deterioration in light conditions and an increased suspension load adversely affecting some species of diatoms. Conversely, some studies have found that even minor volcanic ash deposition events can lead to increased diatom concentrations as silica becomes more bio-available (Lotter et al., 1995; Telford et al., 2004). There was a substantial increase in *D. balfauriana* at 30–32 cm, and this species remained dominant for up to c. 100 years following the deposition of the T2 tephra (Figure 4). Overall, though, changes in the downcore bulk geochemistry had no effect on diatoms species in Kiteschsee Lake (Figure S9, S10).

3. Tephra geochemistry

Downcore shard counting revealed 11 eruption-related airfall tephra peaks distinguishable from the background input of reworked tephra into Kiteschsee Lake (Figure 4, S1, S5). To improve the

tephrochronological framework for the northern Antarctic Peninsula (NAP), we undertook (crypto-)tephrostratigraphic counting on sediments from Kiteschsee Lake and shard-specific geochemical analysis of the two most prominent airfall tephra peaks at 33 cm and 58 cm depth.

Tephra deposits associated with the main eruptions from Deception Island have been mapped out on Deception Island and in lake, marine and ice core records from the NAP, yet gaps in the Mid- to Late Holocene eruptive history and geochemistry of Deception Island remain because analysis in lake sediments and other archives has focused on visible basic (black) tephra horizons which are difficult to differentiate geochemically (Björck et al., 1991c; Hodgson et al., 1998; Smellie, 1999; Roberts et al., 2017; Antoniades et al., 2018). Rhyolite-tephra producing eruptions from Deception Island are less common yet potentially more diagnostic for developing local–regional tephrochronological frameworks.

Deception Island magmas include trachydacitic and rhyolitic compositions, characterised by a high Na_2O content, with post-caldera eruptions more typically exhibiting bi-modal or continuous basalt-andesite to rhyolitic compositions along well-defined alkalinity evolutionary trend (Fretzdorff and Smellie, 2002; Geyer et al., 2019). Rhyo-dacitic tephra deposits on Deception Island are rare (Smellie, 2001), but rhyolitic glass shards have been identified within visible tephra layers of Holocene age from the NAP, and subsequently linked to Deception Island or another eruption from NAP/SSI arc (e.g., Moreton and Smellie, 1998; Fretzdorff and Smellie, 2002; Lee et al., 2007; Roberts et al., 2012, 2017; Geyer et al., 2019). Cryptotephra from large explosive rhyolite-forming eruptions in Southern Patagonia has been identified as far away as South Georgia (e.g., Sollipulli c. 3.0 ka) (Oppedal et al., 2018) and on the Falkland Islands (e.g., Mount Burney, c. 10.0-8.9 ka, Mount Hudson (H2), c. 4.3 ka) (Scaife et al., 2019; Panaretos et al., 2021). Whether tephra from South American eruptions reached the Antarctic Peninsula during the Holocene remains largely unexplored, yet rhyo-dacitic tephra deposits could provide invaluable time-parallel marker horizons, linking palaeoenvironmental records across wide areas of the Southern Ocean (Panaretos et al., 2021).

3.1 Methods

Sub-samples were taken at continuous 0.5 cm intervals for manual shard counting following a modification of the Blockley et al. (2005) 'flotation' protocol to minimise geochemical alteration of the glass shards. The tephra glass-shard fraction was extracted and mounted onto slides with Canada Balsam. Each slide was traversed, and tephra shards were counted, classified and measured at x400 magnification using a high-powered Olympus CX41 microscope.

While most of the 11 above background tephra peaks are composed of dark brown shards of probably basic composition, geochemical analysis of shards from two most prominent airfall peaks at 33 cm and 58 cm depth was prioritised because they are dominated by clear to light brown shards. Shards were handpicked at random using a micromanipulator and mounted in epoxy resin for geochemical analysis. Glass shard geochemistry was analysed using the Cameca SX-100 electron probe microanalyser (EPMA) at the Tephra Analytical Unit, University of Edinburgh, with a beam diameter of 8 µm following procedures in Hayward (2012) and run conditions: 15 keV/2 nA (Al Ka, Si Ka, K Ka, Ca Ka, Na Ka, Mg Ka, K Ka, Ca Ka, Fe Ka); 15 keV/80 nA (P Ka, Ti Ka, Mn Ka, P Ka, Ti Ka). Andradite standards were run at the start and end of each session. Analytical conditions and results for shards with >95% totals are shown in Table S3.

Using the statistical software GCDkit 3.00 (Janoušek et al., 2006) and data analysis in R, we compared our new data to a database of 2,763 distal tephra major element glass shard analyses from the NAP (Moreton and Smellie, 1998; Roberts et al., 2017; Antoniades et al., 2018; Oliva et al., 2019; McConnell et al., 2021), Antarctica (Weaver et al., 1979; Narcisi et al., 2005; Dunbar and Kurbatov, 2011; McConnell et al., 2021), and Southern South America (McCulloch et al., 2001; 2005; 2016; 2019; 2020; 2021; Sagredo et al., 2011, Mansilla et al., 2016; 2018; Stern et al., 2016; Smith et al.,

2019; Blaikie, 2020). Data were filtered to remove totals <97%, where SiO2 <63% (i.e., 'basic-intermediate'), and <95%, where SiO2 >63% (i.e., 'acid'), and recalculated (normalised) to 100% on a 'water-free' basis (Roberts et al., 2007), leaving 2,480 analyses. Analysis was undertaken using R v. 4.1.0/RStudio v. 1.4.1717, with correlations between major elements visualised using bi-plots and correlograms (Figure S14, S15, S16). Multivariate principal components analysis (PCA) and discriminant hierarchical (k-means) clustering were undertaken using nine major elements common to all datasets (SiO_2, TiO_2, Al_2O_3, FeO, MnO, MgO, Cao, Na_2O, K_2O) (Figure S17, S18). Data were square root, centred and standardised (Z-scores) and centred log ratio (clr) transformed. The latter overcomes issues associated with closed sum data.

3.2 Results & Interpretations

Glass shard-specific electron probe microanalysis of the two most prominent tephra horizons showed that an airfall layer at 33 cm depth (KITE_33 or K33 in Figure 4, S1-S5) (1,720 $^{+630}_{-240}$ cal. a BP) had a broadly bi-modal basaltic-rhyolite glass shard geochemical composition, while a thin uni-modal tephra peak at 58 cm depth (KITE_58 or K58) (5,550 $^{+150}_{-200}$ cal. a BP) within a ~6 cm thick tephra deposit at 62 and 56 cm consisted solely of rhyolitic glass shards. Both align with the magma evolution trend of the Deception Island volcano (Figure S1, S5, S14, Table S5), and share geochemical characteristics of post-caldera eruptions (cf. Geyer et al., 2019).

The triple tephra peak between 62 cm and 56 cm depth composed of basic-rhyolitic shards implies a multi-stage eruption occurred at or around 5.5 ka. Multivariate analyses revealed that rhyolitic shards in the 58 cm layer are most similar to NAP tephra layers previously linked to Deception Island, but no close matches to South American eruptions were found. A similarly well-defined and thin rhyolitic horizon in marine core PC460 from the Bransfield Strait has a comparable age to the Kiteschsee Lake 58 cm peak and Yanou Lake T5 tephra (Roberts et al., 2017).

The geochemistry of the 33 cm tephra peak is less diagnostic than the 58 cm tephra peak but also has a closer affinity with NAP tephra layers previously linked to Deception Island (Figure S17, S18, Table S5, S6). The basaltic–andesitic component of the 33 cm tephra peak overlaps with data from all of Deception Island's Holocene basic-andesitic eruption, while its rhyolitic glass shards closely match compositions from the T7 deposit in the Yanou Lake record, deposited c. 7–6 cal. ka BP (Figure S17, S18, Table S5, S6). Evidence of a large eruption is also present at 7–6 cal. ka BP in marine records from the NAP and Scotia Sea (Moreton and Smellie, 1998: tephra A; Xiao et al., 2016: layer A1 in PS67/205-2). We consider a link between the 33 cm tephra peak and T7 to be highly unlikely because diatoms preserved in Kiteschsee Lake sediments between 30-35 cm are all freshwater and sediments older than 7 ka would have been deposited in a marine environment. Therefore, the 33 cm tephra peak is most likely the product of a previously unidentified Late Holocene bimodal eruption (Figure S1, S14-S17; Table S5, S6). Its 95% CI age range of 2,320–1,480 cal. a BP overlaps with the 95% CI age range of 2,390–1,850 cal. a BP associated with the T2 layer in the Yanou Lake record (Figure 4B-D, 5C) (Roberts et al., 2017), and the T2 tephra layer in lake sediments from Barton Peninsula (Oliva et al., 2019). Rhyolitic shards have not yet been analysed in the T2 layer from the Yanou Lake or Barton Peninsula lakes.

Multivariate PCA and cluster analysis of rhyolitic shards from the 33 cm tephra peak, and similar analysis of 'acidic' data highlight how its shard geochemistry is more widely dispersed than the 58 cm tephra peak rhyolitic data, with 68% and 95% confidence ellipses encompassing rhyolitic NAP (Deception Island) (Figure S17, S18). However, a third of the rhyolitic shards analysed have broad compositional similarities to tephra from the Mount Hudson H2 and Solipuli eruptions from South America (Figure S17; Group 2 in Table S6). At this time, we cannot conclusively link the 33 cm tephra to Deception Island. Cryptotephra from the Mount Hudson H1, the Mount Burney MB2 eruptions and other large eruptions from southern South American volcanoes could feasibly exist in

other lake and marine records from the Antarctic Peninsula. Further application of the cryptotephra methodology and further major and trace element analysis of shards in lake sediment records from across the South Shetland Islands is recommended.

3.3 Tephra layers and Deception Island eruption history

The geochemistry of glass shards from two most prominent tephra layers in Kiteschsee Lake, at 58 cm depth (5,560 $^{+160}_{-220}$ cal. a BP; T5) and 33 cm depth (1,720 $^{+630}_{-240}$ cal. a BP; T2) show that rhyolite-forming eruptions from the Deception Island volcano could have occurred regularly in the Mid- to Late Holocene. Geochemically, the eruptive history of the Deception Island volcano has been dominated by basalt to basalt-andesite tephra producing events of varying magnitudes (Björck et al., 1991c; Mäusbacher et al., 1989; Moreton and Smellie, 1998; Tatur et al., 1999; Roberts et al., 2017; Geyer et al., 2019, with post-caldera eruptions characterised by diagnostic basalt-andesite to rhyolitic compositional trend (Geyer et al., 2019). Glass shards within tephra layers such as the T7 layer, dated in the Yanou Lake record to 7,410–6,120 cal. a BP (95% CI range) (Roberts et al., 2017) have a broadly bi-modal composition, and a rhyolitic component that also follows this evolutionary trend (Figure 3A).

Roberts et al. (2017) postulated either the Yanou Lake T7 or T5 layers might be the products of a large caldera-forming eruption, or an eruption induced partial collapse of Deception Island. The Deception Island 'caldera-forming' event was originally linked to pre-Holocene or Early Holocene bi-modal tephra horizons in marine records from across the Peninsula and Scotia Sea and termed the 'Megascopic' event (Moreton and Smellie, 1998; Smellie, 2001). Ages from these widespread deposits are similar to the c. 10 cal. ka BP age of the T10 tephra deposit in the Beak Island Lake 1 record (Roberts et al., 2011; Sterken et al., 2012) and the T7 event in the Yanou Lake record (7.4–6.1 cal. ka BP; 95% CI age range).

Radiocarbon ages of aquatic moss below and above the T5 of c. 5.5–4.7 cal. ka BP, respectively, in Yanou Lake are similar to ages of the most substantial tephra deposits and gravity flows (>0.5 m thick) preserved in nearby sediment records from Ardley Lake, Belen Lake, Gaoshan Lake and Long Lake (Roberts et al., 2017). Aquatic moss immediately below the T5 tephra deposit provide the most reliable eruption age constraints because ages from aquatic moss above tephra deposits more likely reflect the timing of lake ecosystem recovery. A substantial lake reservoir offset of >1,500 years seems unlikely in the Mid- to Late Holocene parts of the Yanou Lake record as radiocarbon ages between c. 4.7 cal. ka BP and the present day are in sequence and all ages were obtained from a species of aquatic moss with no modern age offset. The T5 tephra layer in the Yanou Lake and Kiteschsee Lake records has a similar age to the T3/4 tephra layer in lake sediments from Barton Peninsula (Oliva et al., 2019) and the c. 5.5 cal. ka BP age from the T5 layer in lake sediments extracted from Byers Peninsula, Livingston Island (Antoniades et al., 2018).

Based on radiocarbon dating of aquatic moss layers above a seismic deposit in lakes on Byers Peninsula, Livingston Island Antoniades et al. (2018) suggested the largest eruption from Deception Island of the Holocene and its caldera-forming eruption took place at 3,980 ± 125 cal. ka BP. This age is broadly equivalent to the age of the first of three stratigraphically closely-spaced visible tephra layers with a modelled 95% confidence interval age range of 3.5–3.8 cal. ka BP in the Yanou Lake record (T3a in Figure 4, 5C, Table S1B), which we have linked to three stratigraphically closely-spaced visible tephra layers of similar thickness in the Kiteschsee Lake record between 45–40 cm depth, and it also overlaps with the less well-defined T4 tephra layer (3.9–4.4 cal. ka BP). Antoniades et al. (2018) linked the caldera-forming eruption event to the largest interruption of lacustrine sedimentation by gravity flows in Hotel Lake and Tiefersee on the Fildes Peninsula at >c. 4 cal. ka BP and between 3.3–4.3 cal. ka BP, and in Rudy Lake on Potter Peninsula, between 3.8 and 5.2 cal. ka BP. Rapidly-deposited gravity flow sediments of similar thickness also exist in Ardley Lake, Belen Lake, Gaoshan Lake and Long Lake (Watcham et al., 2011; Roberts et al., 2017), but are all older

than c. 4.7 cal. ka BP. No such disruption to lacustrine sedimentation was found in the Kiteschsee Lake sediment record examined in this study.

Multiple caldera collapses in the Holocene are considered unlikely due to the amount of time needed to fully recharge the magma chamber (Geyer et al., 2019; Smellie, pers. comm.), which implies that explosive rhyolitic eruptions were generated by magma injection processes (Geyer et al., 2019) and/or enhanced magmatic interaction with seawater (Forte and Castro, 2019). Like the rest of the South Shetland Islands, Deception Island experienced crustal and magma chamber stress associated with changes in sea level and ice unloading that potentially triggered explosive volcanic activity (Satow et al., 2021).

Taking all the available sedimentological and chronological information into account (including dating uncertainties and potential reservoir effects), it seems likely that the Deception Island caldera-forming event occurred sometime between c. 5.6–3.8 cal. ka BP. In the context of deglaciation and isostatic rebound, it is interesting to note that a c. <5.6 ka age for the Holocene caldera-forming event of Deception Island occurred shortly after deglaciation of the Bellingshausen Ice Cap to within its present-day limits on King George Island (cf. Maclennan et al., 2002; Praetorius et al., 2016).

4. Data availability

Datasets generated in this study are included in the main text and Supplementary Materials and are available from the NERC EDS UK Polar Data Centre (https://www.bas.ac.uk/data/uk-pdc/), on request from polardatacentre@bas.ac.uk and sjro@bas.ac.uk, and in the doi links below. Code, data, and package references are also available on https://github.com/stever60/Fildes_Peninsula.

Heredia Barion, P., Strelin, J., Spiegel, C., Binnie, S., Wacker, L., Pearson, E., Bentley, M., Hocking, E., Roberts, S. (2023). *Chronostratigraphic data constraining Holocene glacial readvance from the Fildes Peninsula, South Shetland Islands, northern Antarctic Peninsula.* (Version 1.0) [Data set]. NERC EDS UK Polar Data Centre. https://doi.org/10.5285/b73794b8-5874-4c51-a2f2-fa895553dfcb

Heredia Barion, P., Strelin, J., Spiegel, C., Binnie, S., Wacker, L., Pearson, E., Bentley, M., Hocking, E., Roberts, S. (2023). *Data compilation for Holocene glacial readvance from the Fildes Peninsula, South Shetland Islands, northern Antarctic Peninsula.* (Version 1.0) [Data set]. NERC EDS UK Polar Data Centre. https://doi.org/10.5285/a89028f1-76d0-41f4-bee0-021633a8b0ed

Roberts, S., Pearson, E., Davies, J., Jones, V., Gabriel, I., Blockley, S., Davies, S., & Roland, T. (2023). *Sedimentological, geochemical, biological, and chronological data from a sediment core record extracted from Kiteschsee Lake, Fildes Peninsula, South Shetland Islands, northern Antarctic Peninsula.* (Version 1.0) [Data set]. NERC EDS UK Polar Data Centre. https://doi.org/10.5285/E117045D-AB43-4D0D-9E14-5B6D9A03B301

Roberts, S., Pearson, E., Gabriel, I., Blockley, S., Foster, I. (2023). *Reconstructed temperature and tephra deposit age data from Yanou Lake, Fildes Peninsula, South Shetland Islands, northern Antarctic Peninsula.* (Version 1.0) [Data set]. NERC EDS UK Polar Data Centre. https://doi.org/10.5285/621cf434-1517-4b36-887d-4285315af695

Roberts, S., Saunders, K., (2023). *Proxy data from the Emerald Lake sediment record on Macquarie Island.* (Version 1.0) [Data set]. NERC EDS UK Polar Data Centre. https://doi.org/10.5285/85c30cc3-6ce6-4a3d-be60-0bddbe69e5bb

5. Supplementary Figures and Tables
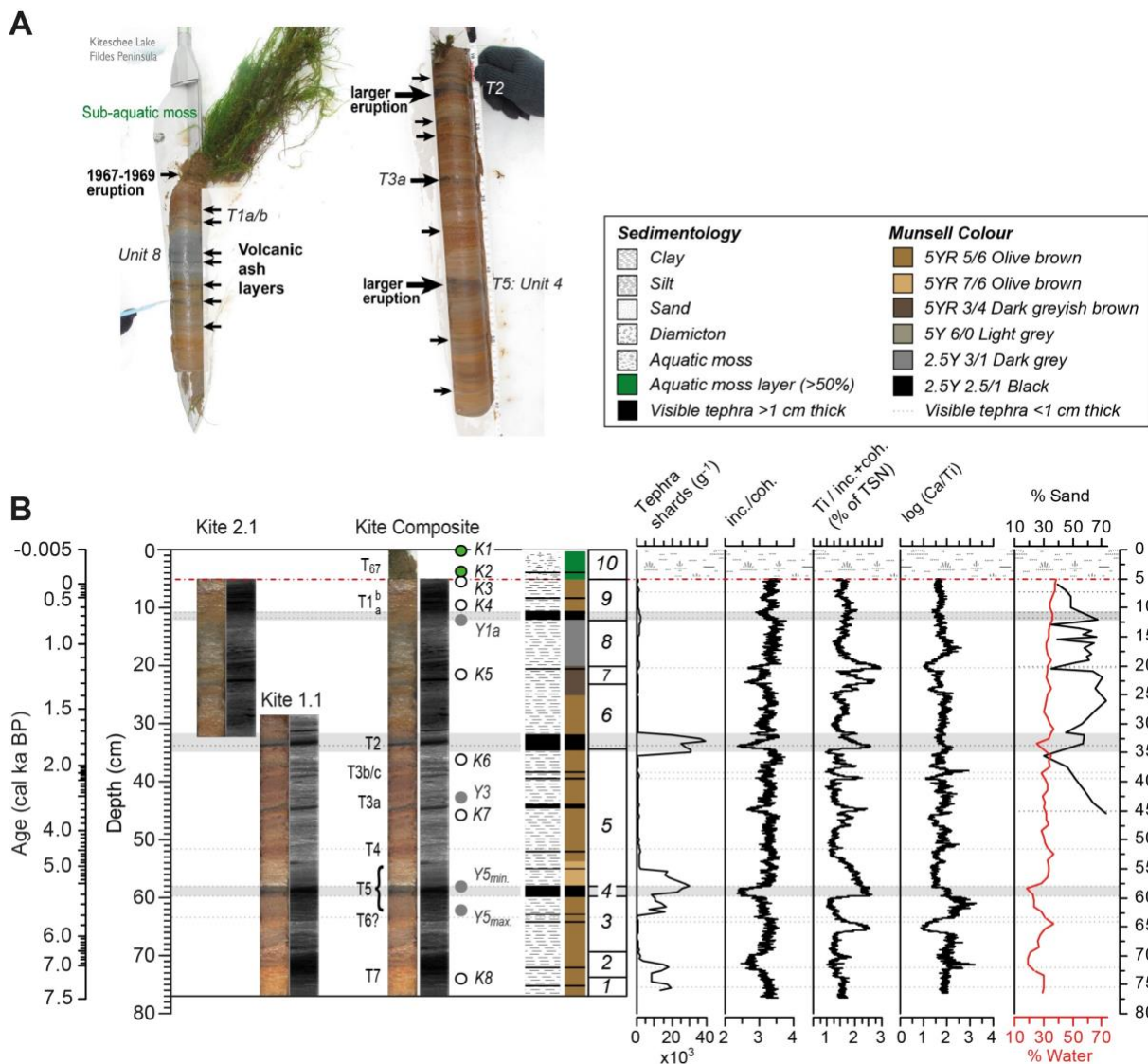
Figure S1. A) Field photograph showing visible tephra layers in both Russian cores taken from lake-ice on Kiteschsee Lake in November 2011 CE and thick living aquatic moss at the sediment-water interface. The living moss and the top 5 cm of the core Kite 2.1 is composed of intercalated moss and sediment and was removed from the top of Kite 2.1 in the field to avoid contamination. The two thickest tephra layers marked 'larger eruption' in A include KITE_33 and KITE_58 are shown as T5 (62–57 cm) and T2 (33 cm) in this diagram. A tephra layer within aquatic moss that returns a post-bomb age reflects the last large eruption from Deception Island that began in 1967 CE. B) Alignment of Russian cores Kite 2.1 (33.5 cm) and Kite 1.1 (48.5 cm) into a 77 cm long composite record and location of radiocarbon dating samples and key lithological and geochemical data from the Kiteschsee Lake record. In order, left to right: Tephra layers and radiocarbon dating samples K1–K8. XRF-CS_ITRAX optical image and X-radiograph (positive image); summary lithology and RGB Munsell colour; lithofacies units 1–10 defined by CONISS cluster analysis of micro-XRF data and key geochemical and sedimentological parameters measured.
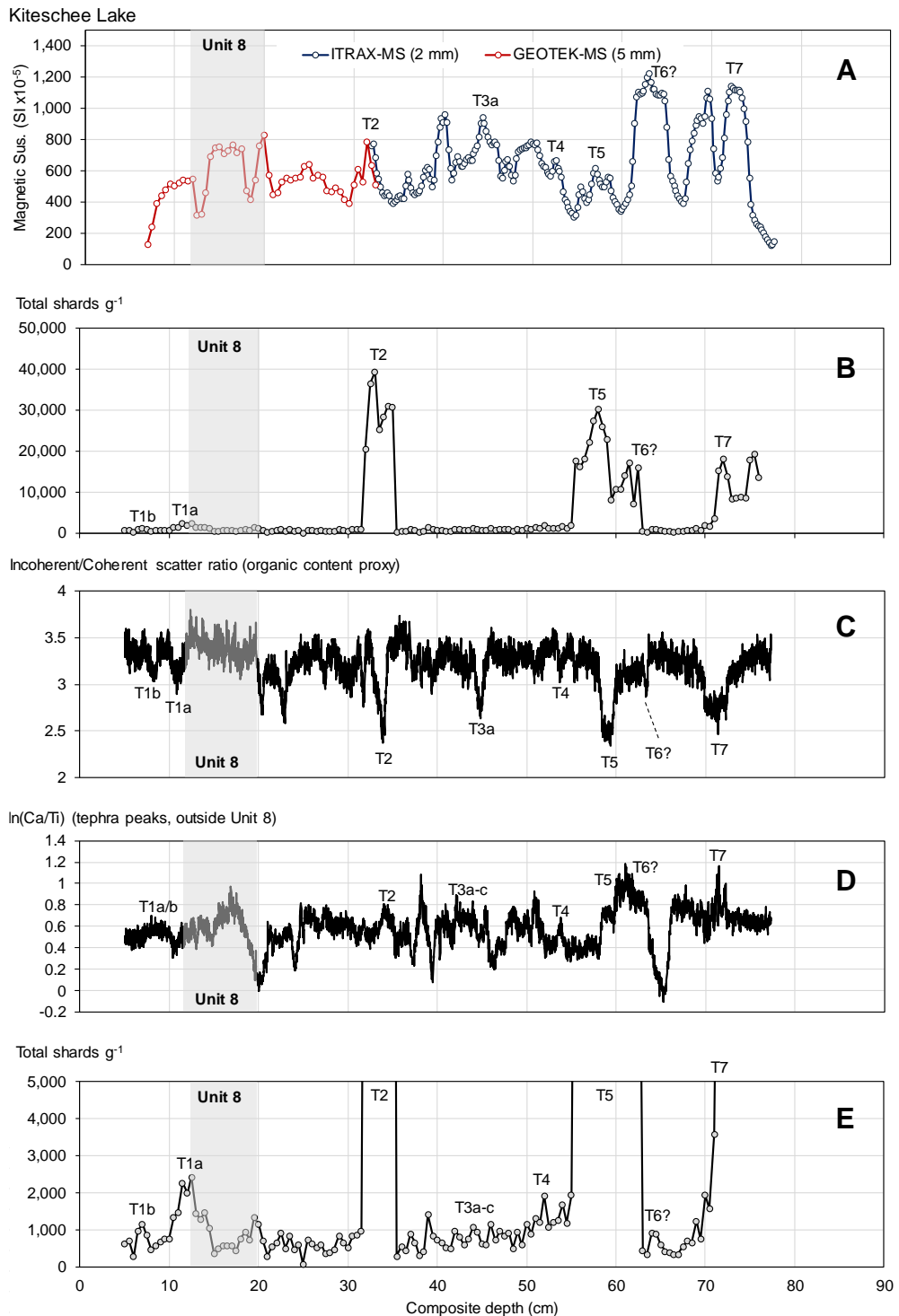
Figure S2. A) Magnetic susceptibility data used to align Kiteschsee Lake sediment Core 1 (27.5 cm) and Core 2 (51 cm) at 31 cm composite depth. The 0-5 cm surface moss layer (lithofacies unit 10) was not included in core-scans. B) Summary tephra shard count data undertaken at 0.5 cm intervals for the 77 cm long Kiteschsee Lake composite core. C) Incoherent/coherent ratios measured contiguously at 200 μm intervals by XRF-CS. The inc./coh. ratio has been used widely as a proxy for changes in organic content (Davies et al., 2015). Airfall tephra has zero to minimal organic content, hence inc./coh. ratio minima provide a precise core depth for airfall tephra deposition in the Kiteschsee Lake record. D) Variations in the Ln(Ca/Ti) ratio. Basic airfall ash is enriched in Ca-rich compared to the surrounding volcanic bedrock, meaning Ln(Ca/Ti) peaks can be used in combination with inc./coh. minima outside of Unit 8 to determine the precise location of (black) airfall tephra layers in the Kiteschsee Lake record. E) Total shard counts between 0–5,000 shards per gram. This plot demonstrates the background level of tephra deposition in the Kiteschsee Lake record.
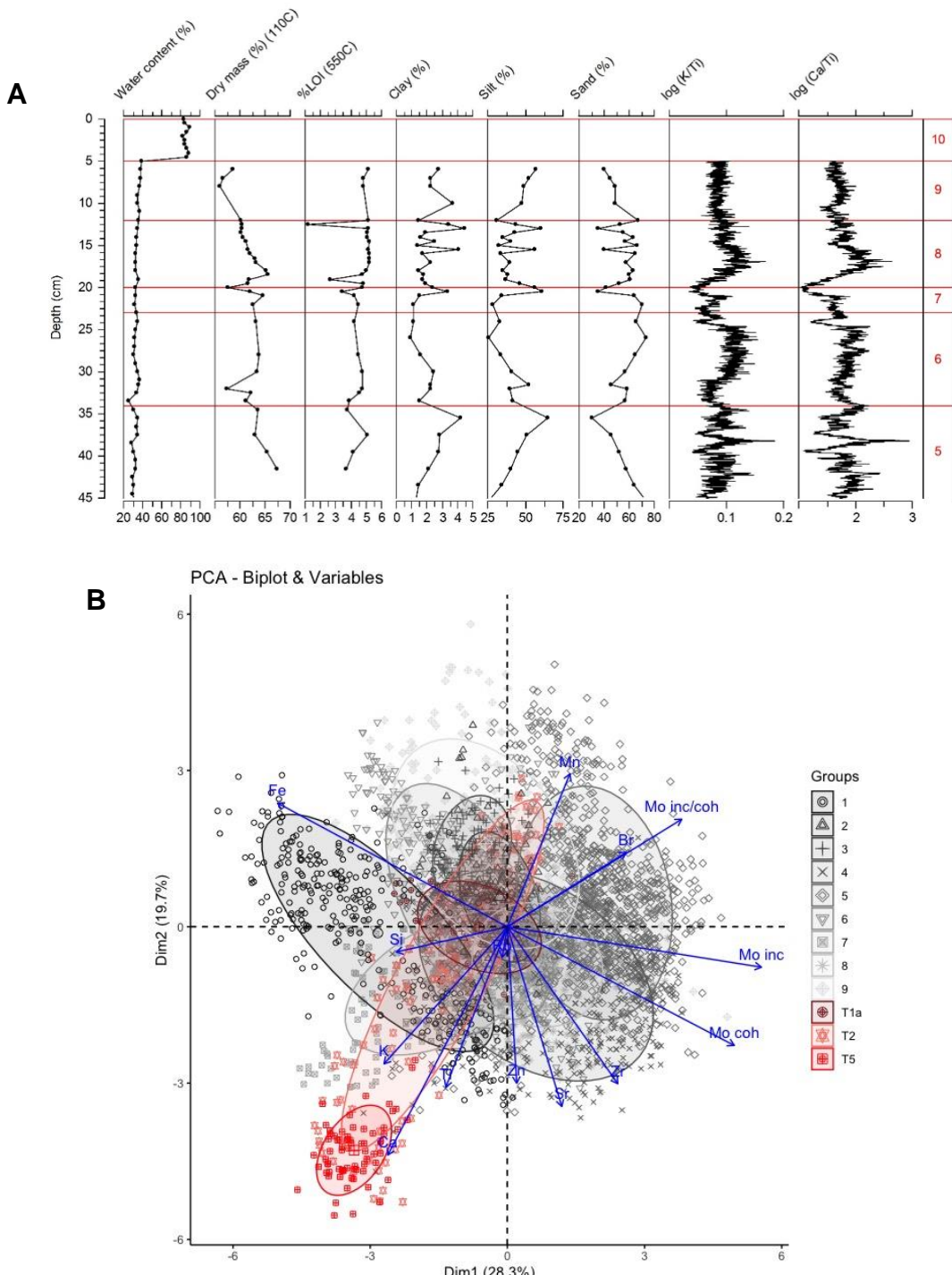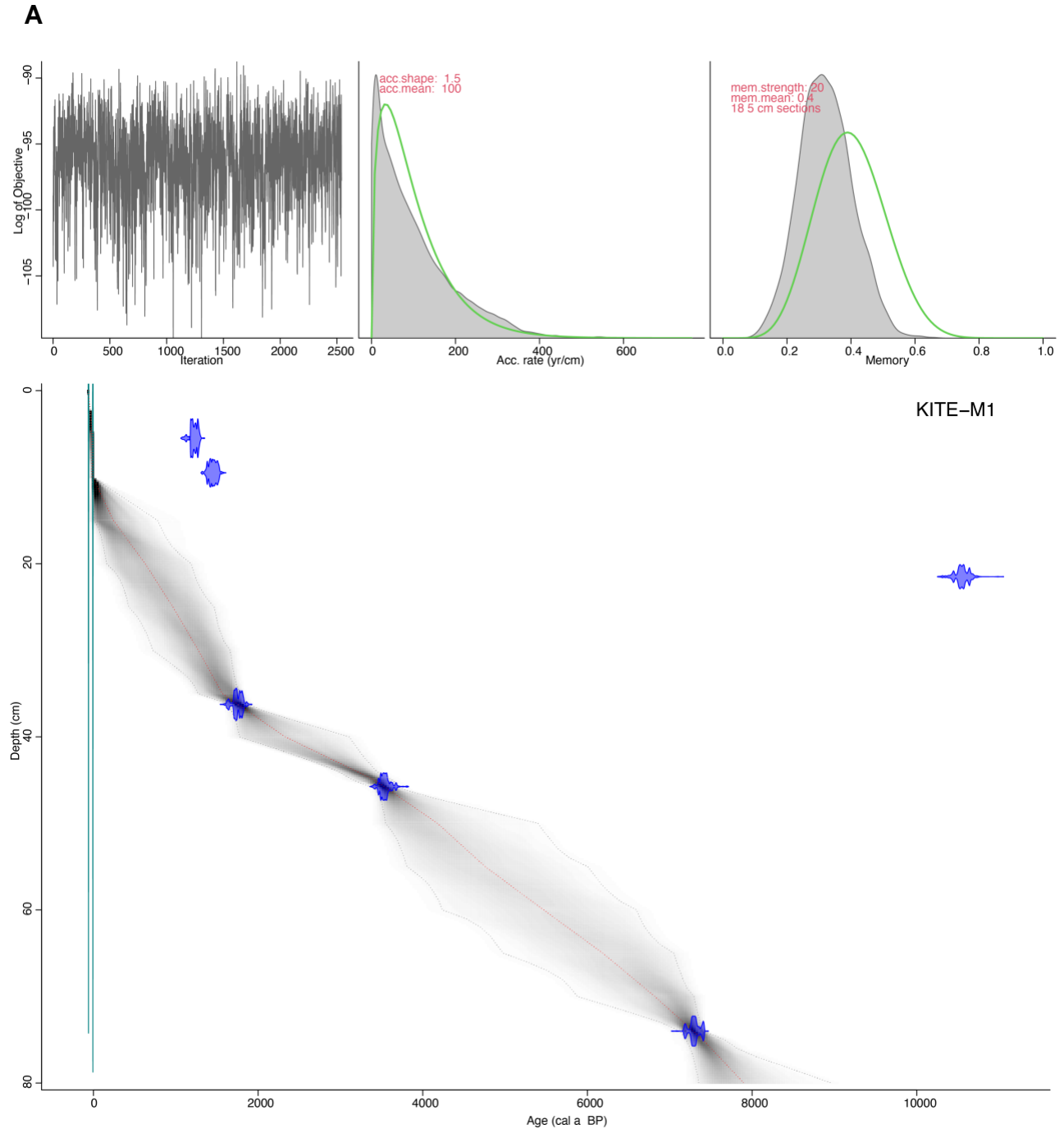
Figure S3. A) Down-core changes in water content, dry mass, %LOI 550 °C (organic matter), grain size[23], log (K/Ti), log (Ca/Ti) and their relationship to Lithofacies Units 5-10 where diatom counting analysis was undertaken. Unit 10 is living aquatic moss attached to the sediment substrate of Unit 9. Organic matter content was generally very low (<6% LOI 550C) and relatively stable throughout the record. Grain size analysis of the core indicates that its sediment is dominated by silt and sand with consistently low clay content (∼3–10%). The silt (sand) component gradually increases to 61% (decreases to 20%), peaking at 35 cm, before declining (increasing) gradually to 23 cm (KITE-M4: 1,420±280 cal. a BP). Silt (sand) content remains stable from 23 cm upwards, but has four sharp peaks (troughs), at 20, 16, 15, and 13 cm depth (1090, 930, 880, 800 cal. a BP). Silt (sand) content gradually increases (decreases) towards the top of the core. B) Principal Components Analysis (PCA) PC2 vs PC1 biplot with 95% confidence ellipses for each unit and tephra layers T1a, T2, T5 of 200-micron XRF-CS scan data from the Kiteschsee Lake sediment record, showing that the bulk

composition of the 58 cm (T5) tephra layer, and to an extent the 33 cm (T2) tephra layer, which are dominated by rhyolitic glass shards are characterised by elevated Ca, K and low inc./coh., Br, Mo. The 58 cm (T5) layer plots in the negative quadrant of the PC1 and PC2 bi-plot and has a geochemical grouping distinct from the bulk geochemistry of Units 1–9.

A
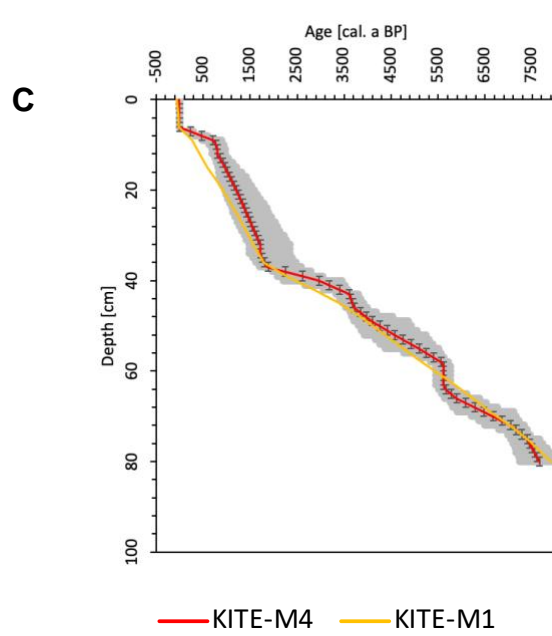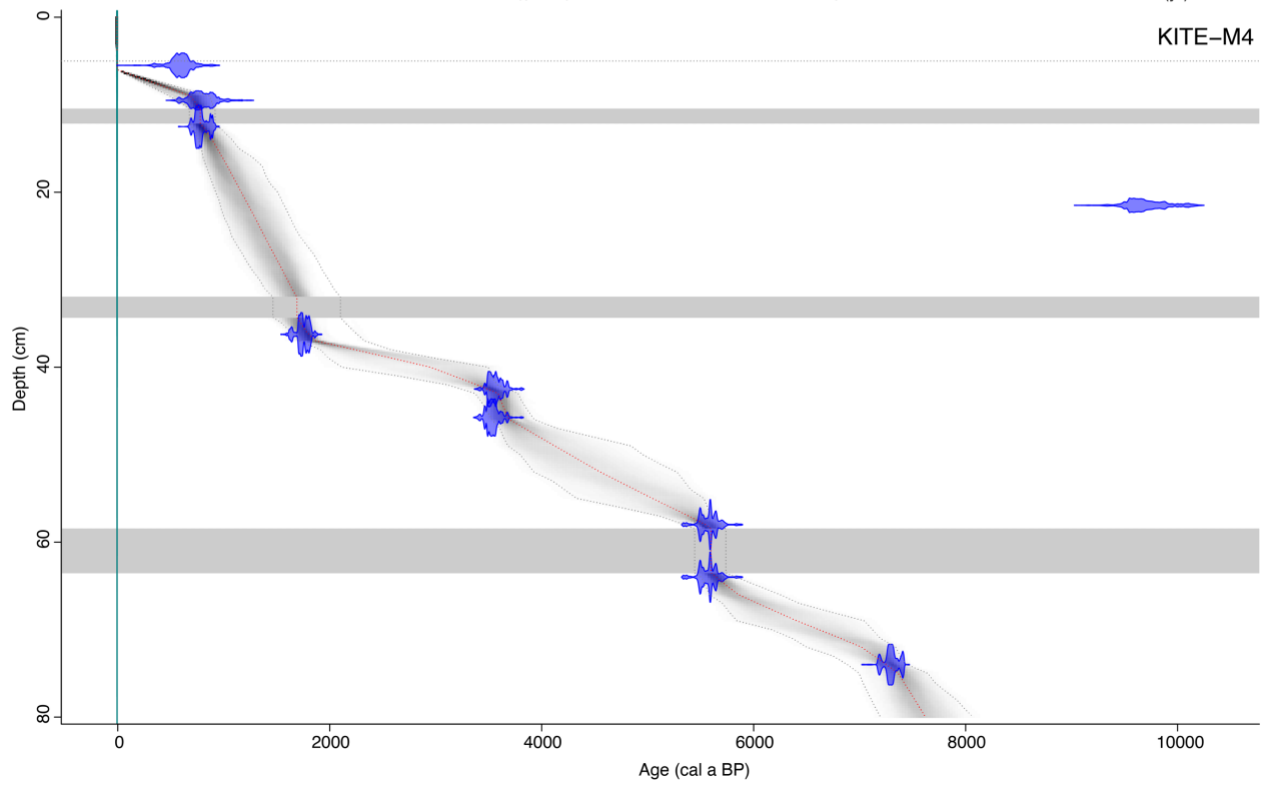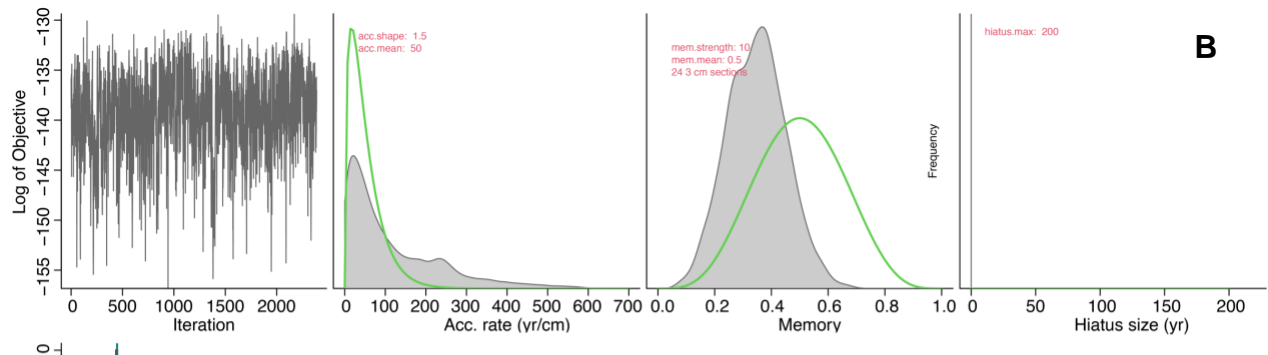
Figure S4. A) KITE-M1 BACON age-depth model and run settings. B) KITE-M4 BACON age-depth model and run settings. C) Comparison of BACON age depth model weighted mean age outputs from the original KITE-M1 and final, tephra-tuned, KITE-M4 age model, highlighting broad similarities within errors.
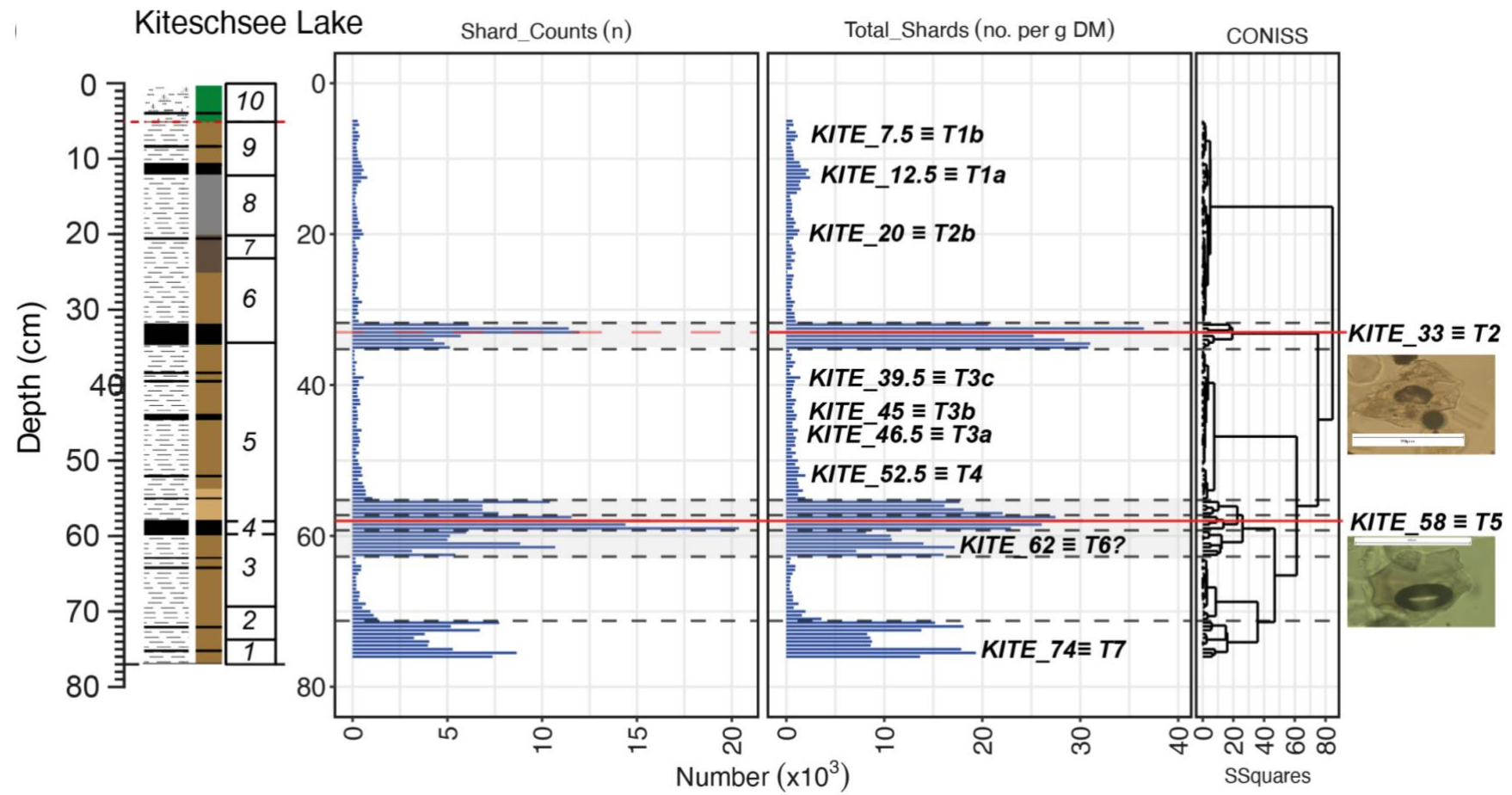
Figure S5. Total glass shard counts cryptotephra analysis. Glass shards which were separated and analysed by electron probe microanalysis (EPMA) were sampled from the two most prominent peaks (KITE_33 (K33) and KITE_58 (K58)). Electron microprobe data from these layers are shown in Table S1 and plotted in Figure 4. Tephrostratigraphic correlations with the Yanou Lake record are labelled as KITE_33 ≡ T2, KITE_58 (K58) ≡ T5, and KITE_74 (K74) ≡ T7 etc. No tephra counts were undertaken on the upper 5 cm aquatic moss layer of Unit 10. The scale bar in the shard photographs is 80 microns.
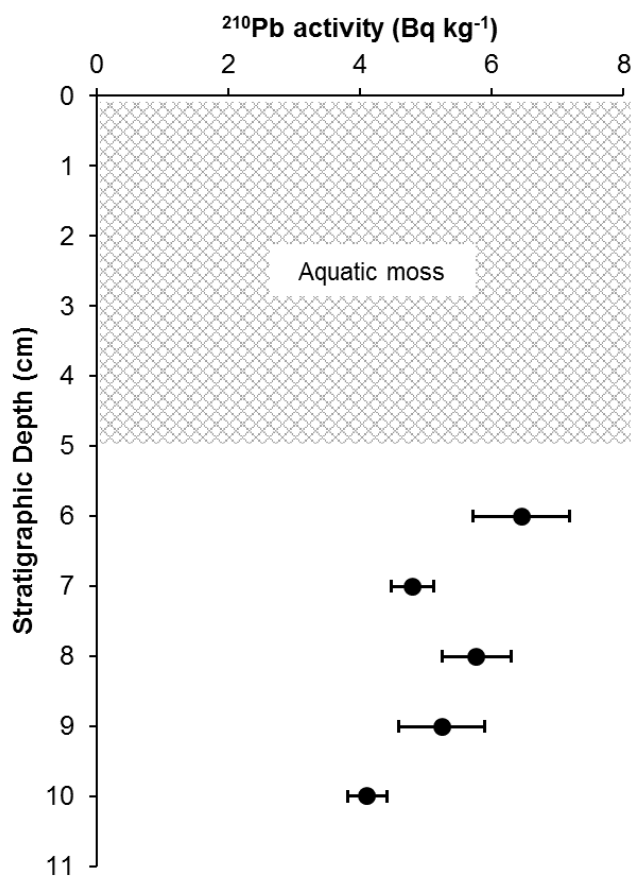
Figure S6. Pb-210 activity levels measured on Unit 9 bulk sediments immediately below the aquatic moss of Unit 10.

Kite 200 um: TSN Z–scores Correlogram by unit defined by CONISS
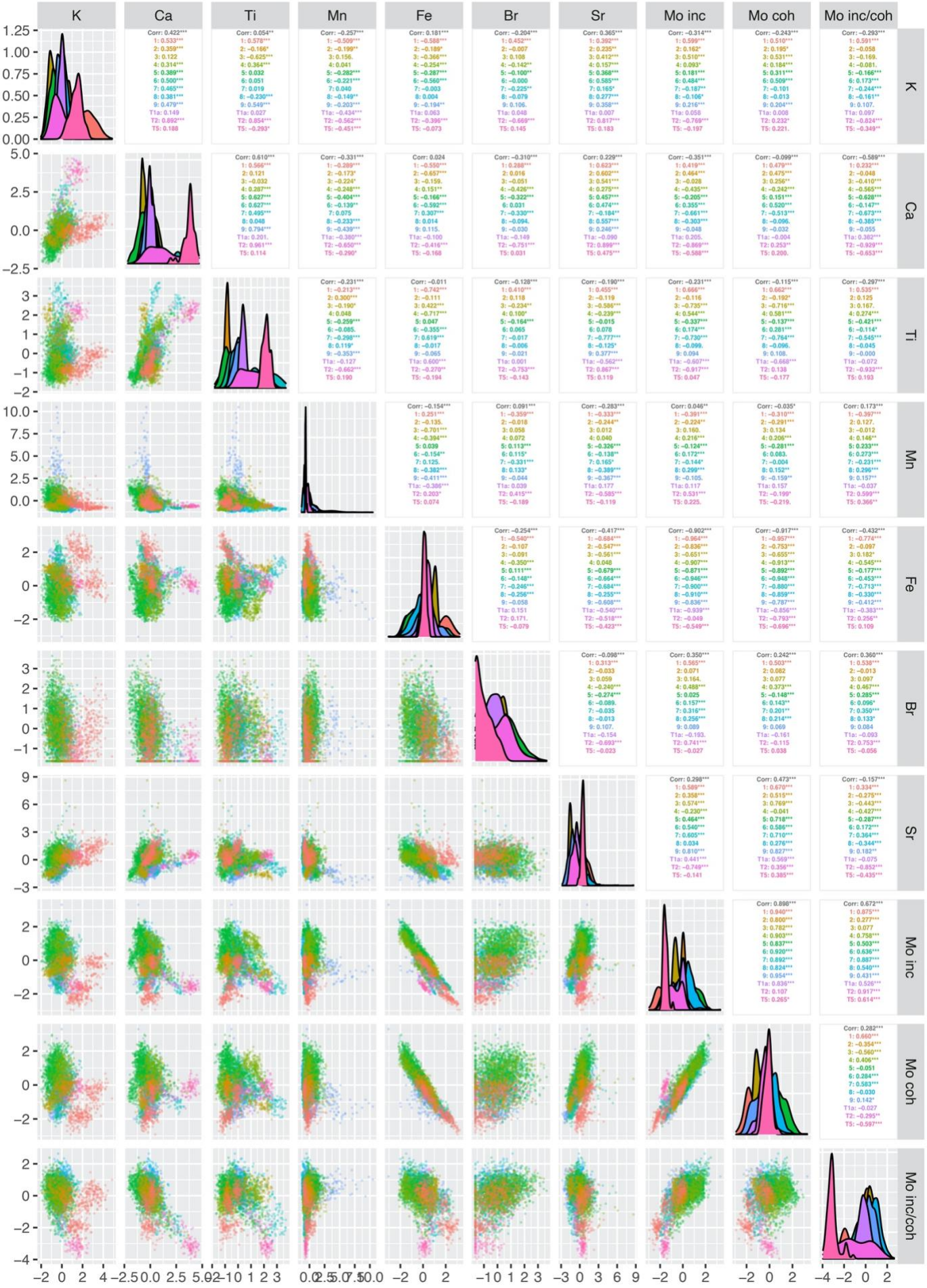
Figure S7. Correlogram for key TSN elements and scatter parameters from micro-XRF scanning of the Kiteschsee Lake record (200 microns). Colours represent the different lithofacies units and tephra layers T1a, T2, T5 as shown in Figure S5.
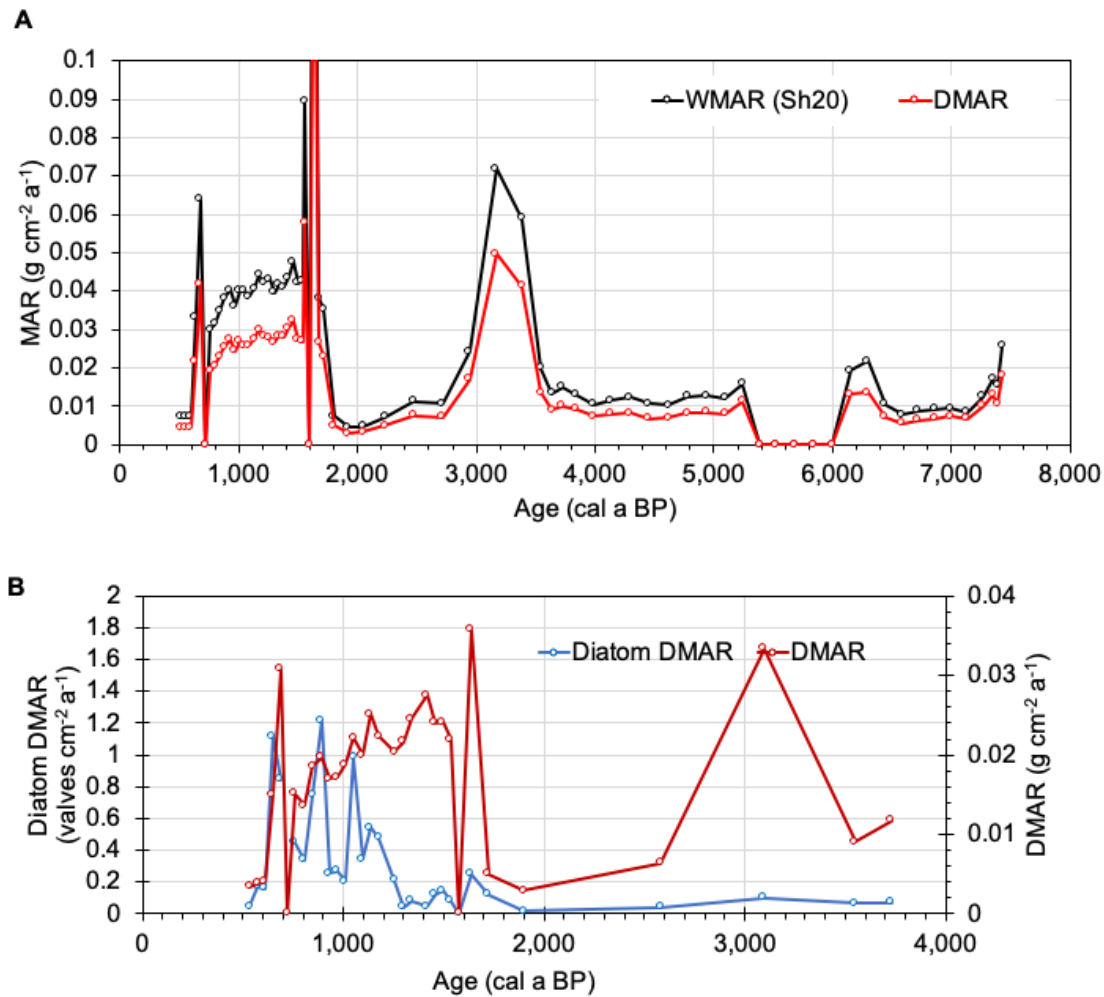
Figure S8. A) Wet and dry mass sediment accumulation rates (WMAR including pore water; DMAR) for the last 8,000 years in the Kiteschsee Lake record (1 cm resolution WMAR and DMAR, g cm^{-2} a^{-1}). B) Diatom dry mass accumulation rate (DMAR) and bulk dry mass accumulation rates for the last 4,000 years (unit 10, aquatic moss, is not included). The most significant upshift in DMAR occurred shortly after 2,000 cal. a BP and coincides with a shift to a colder reconstructed summer air temperatures in the Yanou Lake record (Figure 5G, S11). DMAR remained high and diatom DMAR fluctuated during the meltwater-discharge dominated lithofacies unit 8 between 1,300–700 cal. a BP in the Kiteschsee Lake record.
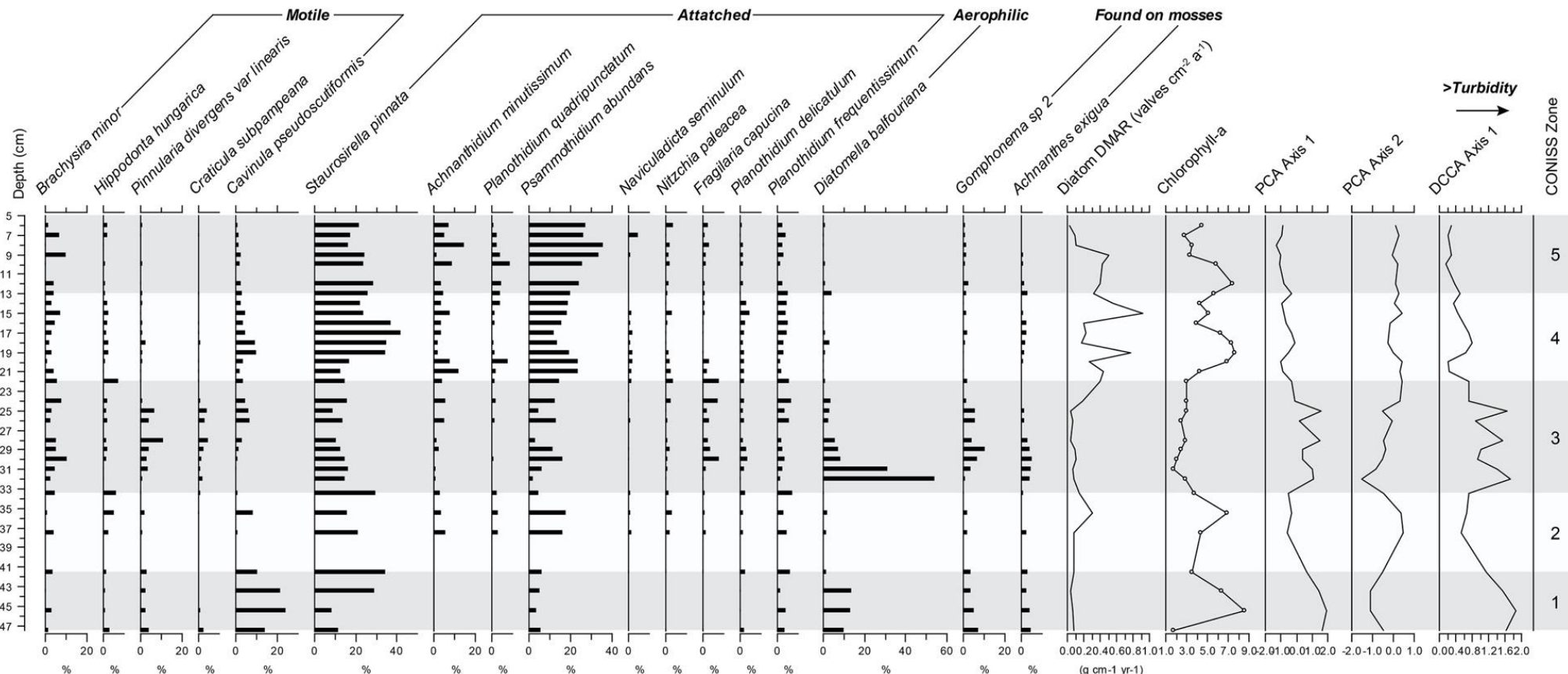
Figure S9. Relative percentage abundances of the most abundant (>2%) diatom species in the Kiteschsee Lake record and diatom concentration, reconstructed chlorophyll-a (from WA inverse transfer function), PCA axis 1 and 2 and DCCA Axis 1 (higher values are warmer temperatures) scores. Five diatom zones were identified using CONISS as follows: Zone 1 = 41.5–47 cm, 2710–3730 cal. a BP; Zone 2 = 33.5–41.5 cm, 1630–2710 cal. a BP; Zone 3 = 22–33.5 cm 1170-1630 cal. a BP; Zone 4 = 13–22 cm (glaciogenic sediments), 800-1170 cal. a BP; Zone 5 = 5–13 cm, 480–800 cal. a BP.
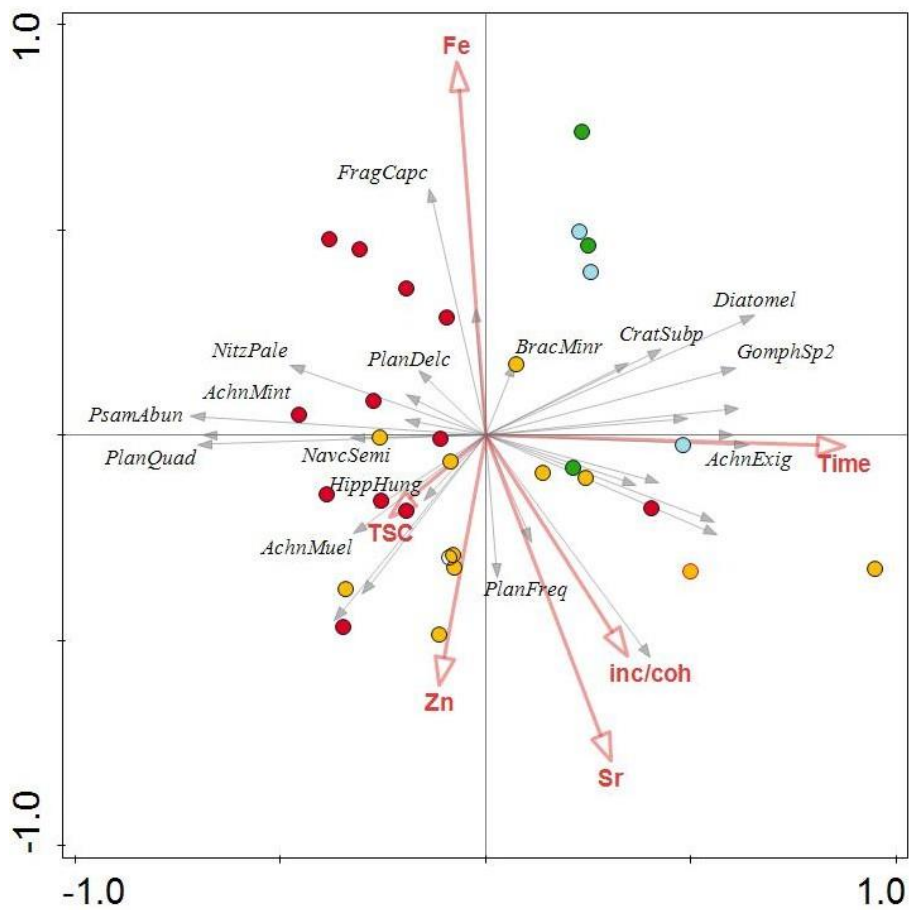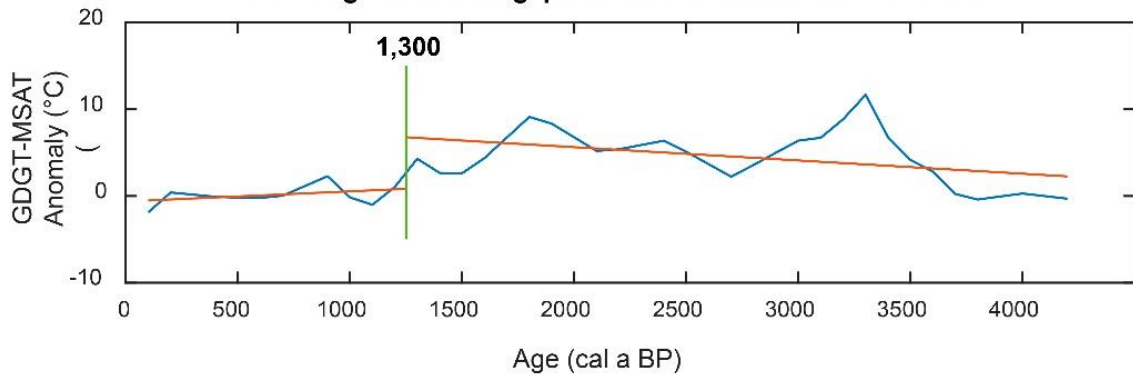
Figure S10. RDA ordination using depth, Zn, Fe, Sr (element/incoherent+coherent as a percentage of the Total Scatter Normalised (TSN) ratio sum; Roberts et al., 2017), incoherent/coherent scatter ratio (inc/coh) from XRF-CS analysis, used here as a proxy for changes in sediment organic and/or water content, tephra shard counts (TSC) and time as explanatory variables (red arrows). Key species are displayed as grey arrows and samples were groups using TWINSPAN (coloured circles).
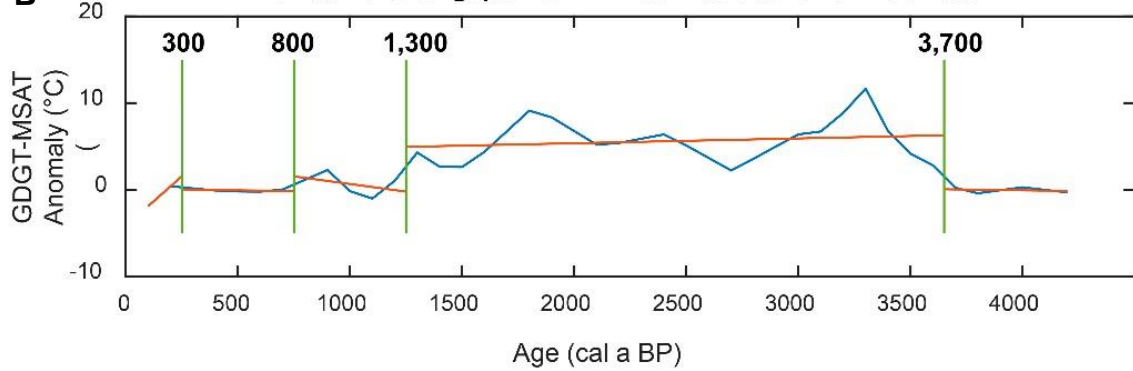
Figure S11. Changepoint time series analysis for the Yanou Lake GDGT-palaeotemperature anomaly record from Roberts et al. (2017). A) The most significant changepoint. B) The four most significant changepoints. Changepoint analysis was undertaken in MATLAB using mean and slope parameters and 0-4 ka standard deviation as the changepoint threshold. Significant changepoints in the mean and slope are shown by green line, with age in years at the top in bold. The red line represents the linear trend for each section.
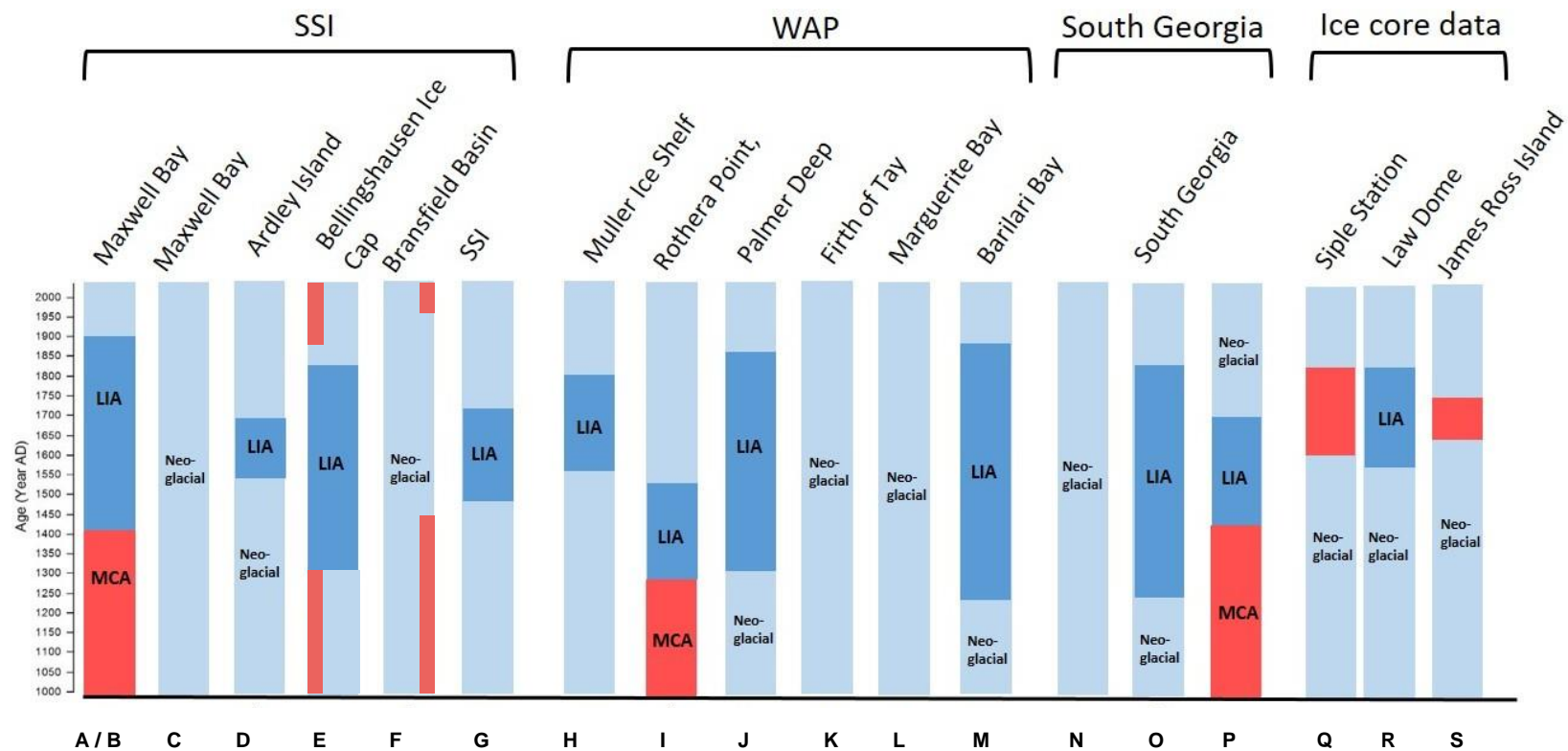
Figure S12. Summary of climate change records from the South Shetland Islands (SSI), Western Antarctic Peninsula (WAP), South Georgia and ice core records from Antarctica. MCA is the Medieval Climate Anomaly, LIA is the 'Little Ice Age'. The 'LIA' is a consistent feature between 1200-1900 CE across the majority of records from the SSI, WAP and South Georgia. References: A) (Monien et al., 2011); B) (Hass et al., 2010); C) (Milliken et al., 2009); D) (Liu et al., 2005); E) (Hall, 2007, 2010); F) (Heroy et al., 2008), (Barnard et al., 2014); G) (Simms et al., 2012); H) (Domack et al., 1995); I) (Guglielmin et al., 2015); J) (Domack et al., 2001); K) (Leventer et al., 1996); L) (Hodgson et al., 2013); M) (Christ et al., 2015); N) (Bertler et al., 2011); O) (Clapperton and Sugden, 1988); P) (Mosley-Thompson et al., 1990); Q) (van der Bilt et al., 2017); R) (Morgan and van Ommen, 1997); S) (Mulvaney et al., 2012).
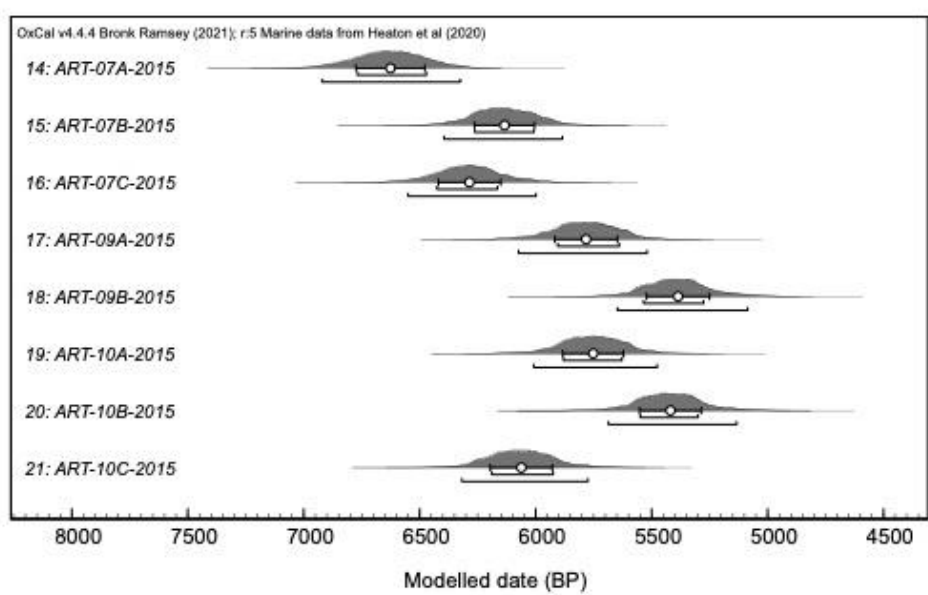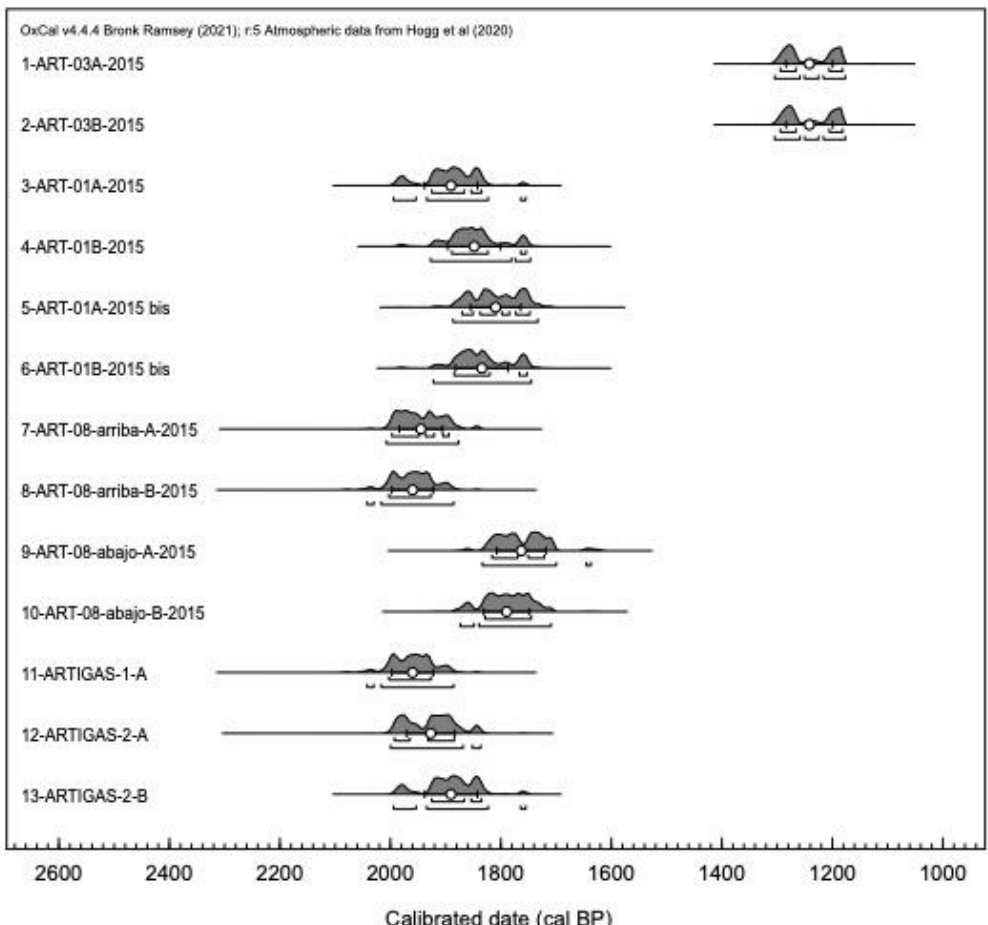
Figure S13. Calibrated radiocarbon ages of new Shetland I moraine samples from Table 1 showing calibrated age probability distribution, mean calibrated ages and one sigma errors (white circle and error bars), and one and two sigma maximum to minimum age ranges beneath.
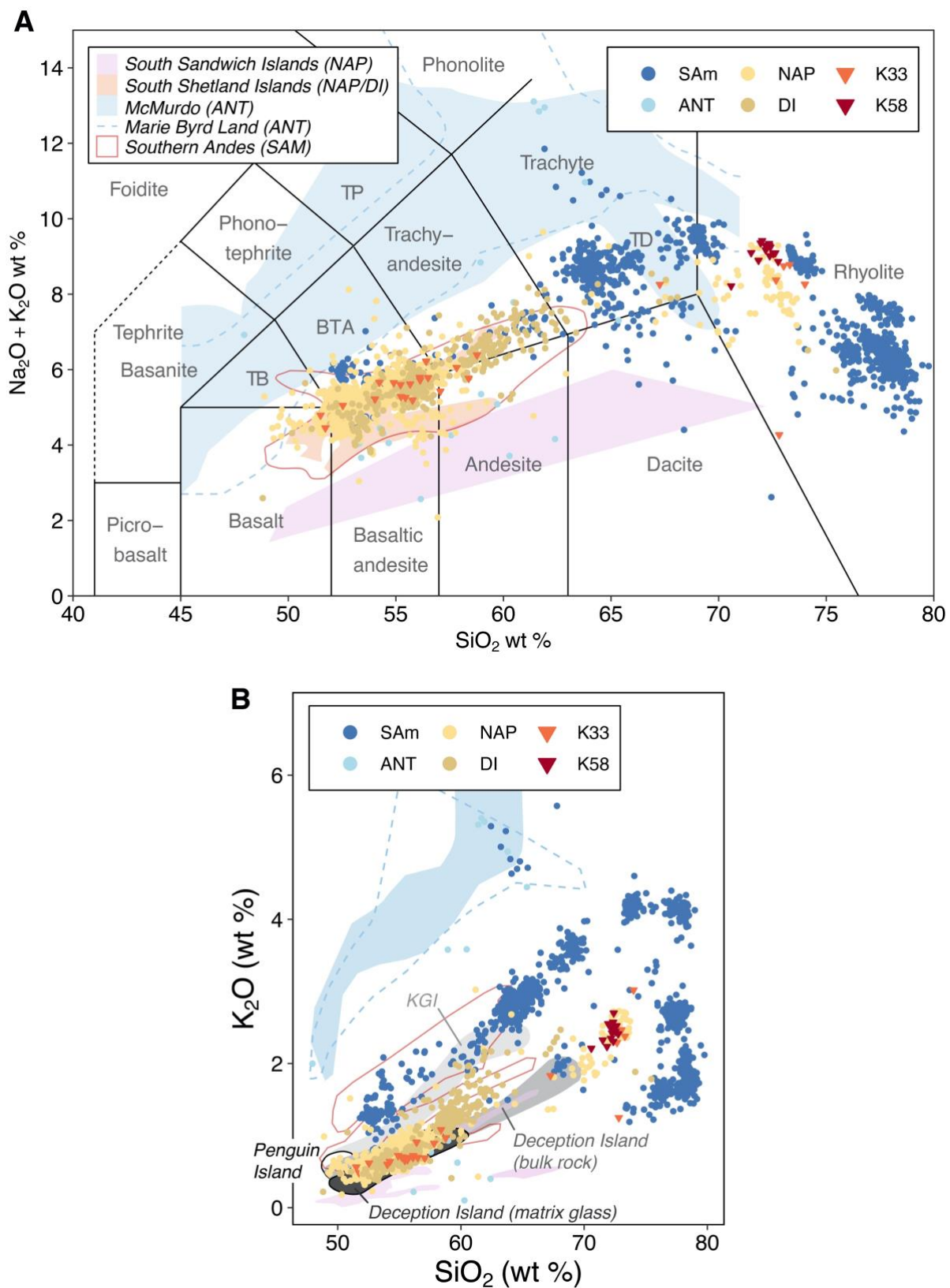
Figure S14. A) Total Alkali Silica (TAS) (Le Bas et al., 1986) and B) K₂O/SiO₂ biplots used to classify and assess potential correlatives for shard geochemical data from 58 cm depth (KITE_58 or K58) and 33 cm depth (KITE_33 or K33) (n = 2,480) (see Data Availability section for links). Sam is South America, ANT is Antarctica, NAP is Northern Antarctic Peninsula, DI is Deception Island. Shaded compositional zones in (A) are based on Narcisi et al. (2005), McConnell et al. (2021), and from Narcisi et al. (2005) and Oliva et al. (2019) in (B). TB is Trachybasalt, BTA is Basalt-trachy-andesite, TP is Tephriphonolite.
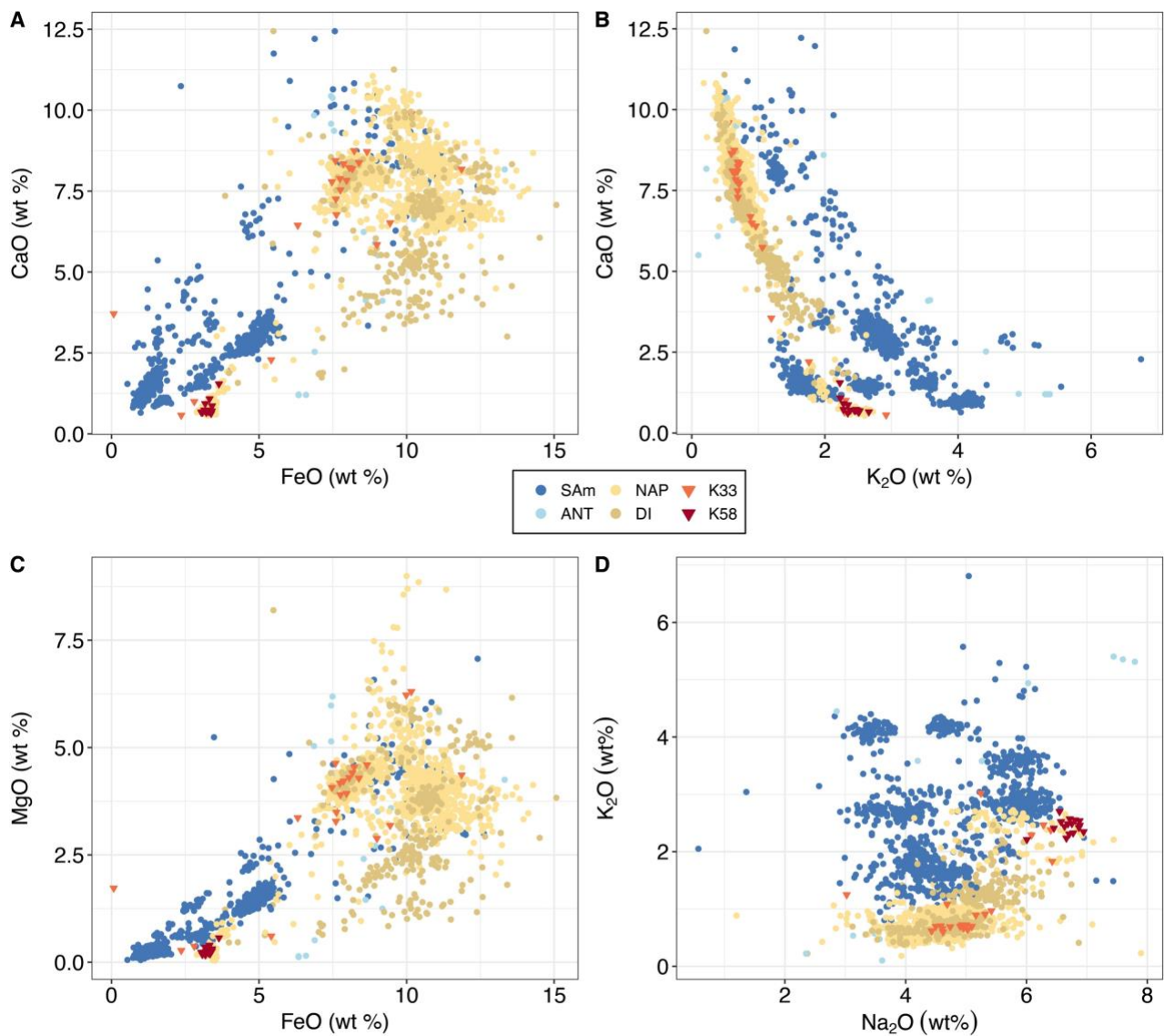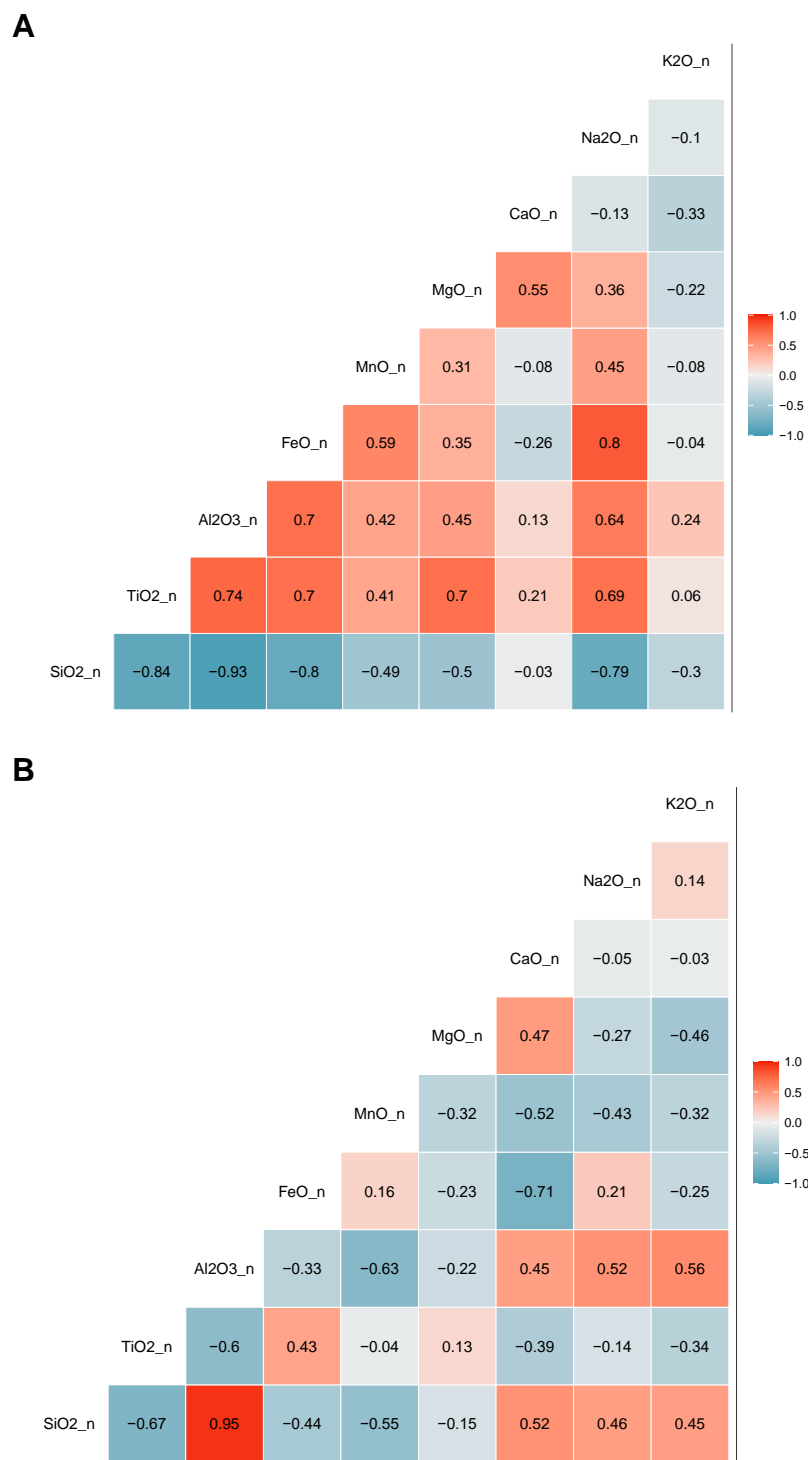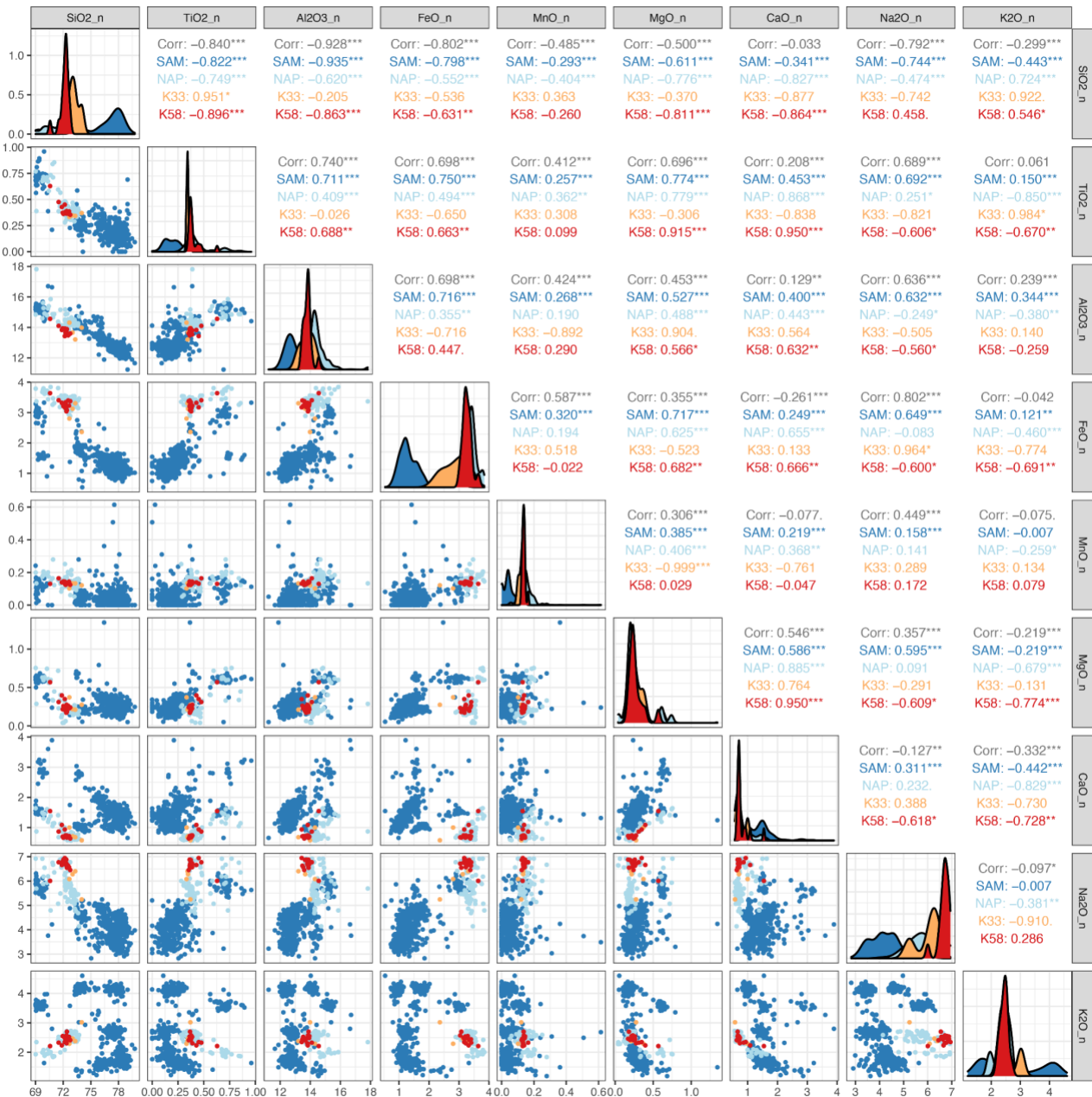
Figure S15. Elemental biplots used to assess potential correlatives for the KITE_58 and KITE_33 shard geochemical data (Table S5; Supplementary Dataset). A) CaO/FeO; B) CaO/K$_2$O; C) Na$_2$O/K$_2$O; D) FeO/TiO$_2$.

Figure S16. Correlation matrices and correlograms (bi-plots, data distribution and correlation matrices) for major element EPMA analysis of rhyolitic glass shards from 33 cm (K33) and 58 cm (K58) depth in the Kiteschsee Lake record and a database of published EPMA rhyolitic glass shard data from the Northern Antarctic Peninsula (NAP), and South America (Sam) (n=622) (datafile available in the Data Availability section). There were insufficient rhyolitic data from Deception Island (DI, n=2) in the database for correlation analysis. A) Correlation matrix for all normalised, square-root, scaled, and centred (Z-scores) transformed data. B) Correlation matrix for all centred log ratio (clr) transformed data, which resolves closed sum effect issues in compositional data (n = 545, rows with infinite values were removed prior to analysis – see R code for details). C) Correlograms for normalised, square-root, scaled and centred (Z-scores) transformed data, plotted by group. D) Correlograms for centred log ratio (clr) transformed data, plotted by group.

C
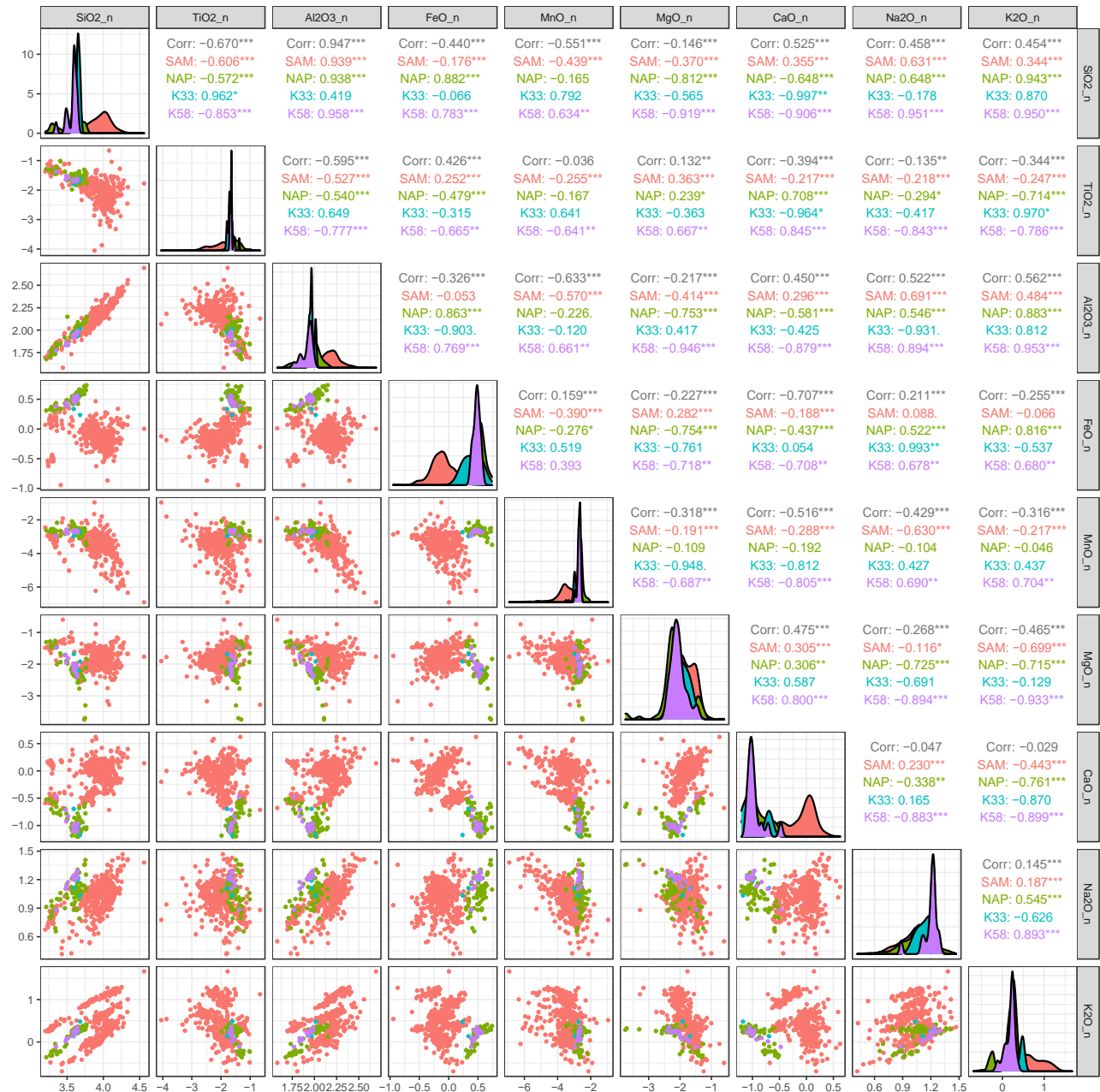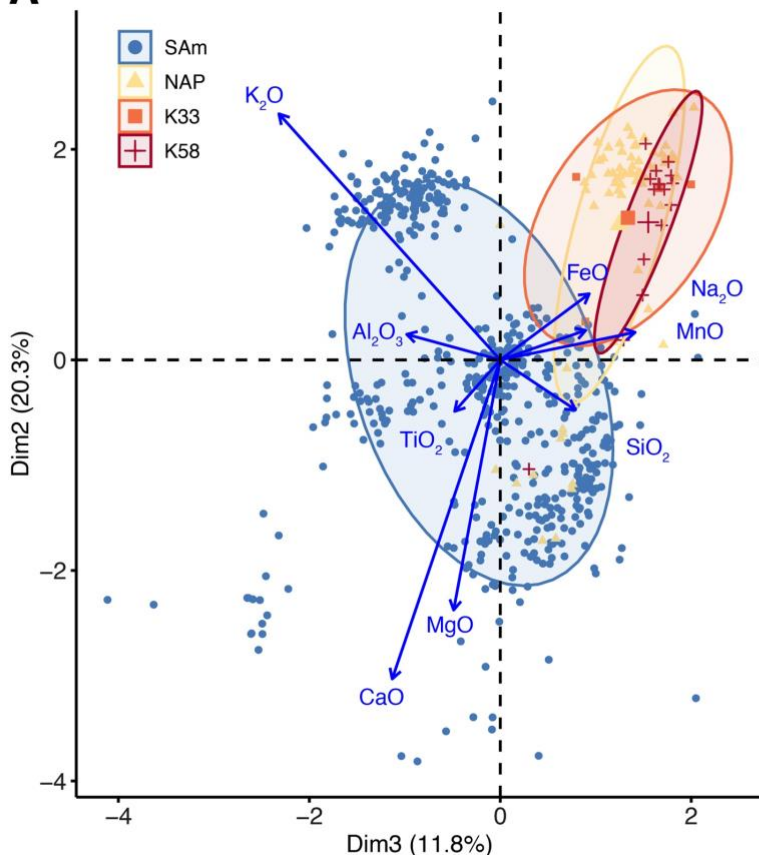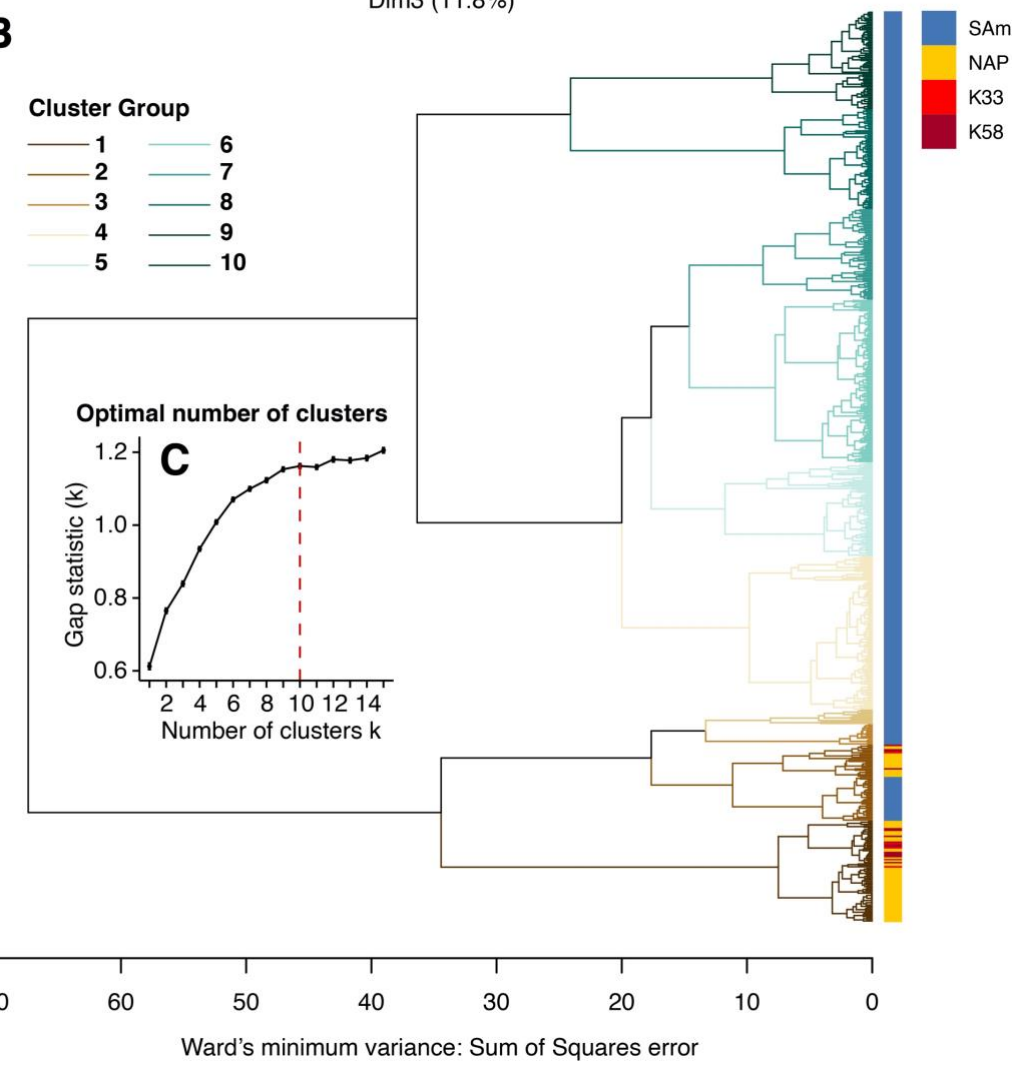
Figure S17 (overpage). A) Principal components analysis showing PC2 versus PC3 biplots of the normalised, square-root, and standardised and centred (Z-scores) transformed major element EPMA rhyolitic glass shard dataset comprising shard data from 33 cm (K33) and 58 cm (K58) depth in the Kiteschsee Lake record, and a database of published EPMA rhyolitic glass shard data from the Northern Antarctic Peninsula (NAP) and South America (Sam) (n=622) (datafile available in the Data Availability section). There were insufficient rhyolitic data from Deception Island (DI, n=2) in the database for PCA analysis. Data were filtered to remove totals <95%. B) Agglomerative hierarchical cluster dendrogram (k-means, Ward's, Euclidean distance) of dataset described in panel A. C) The optimal number of cluster groups. This was defined using the gap statistic, which compares the intra-cluster variation in the number of groups to a reference distribution with no clear clustering and is generated by Monte Carlo simulations with bootstrapping (Tibshirani et al., 2001). Group members are listed in Table S5.

A PC2/PC3 and Variables (68% Confidence Ellipses)
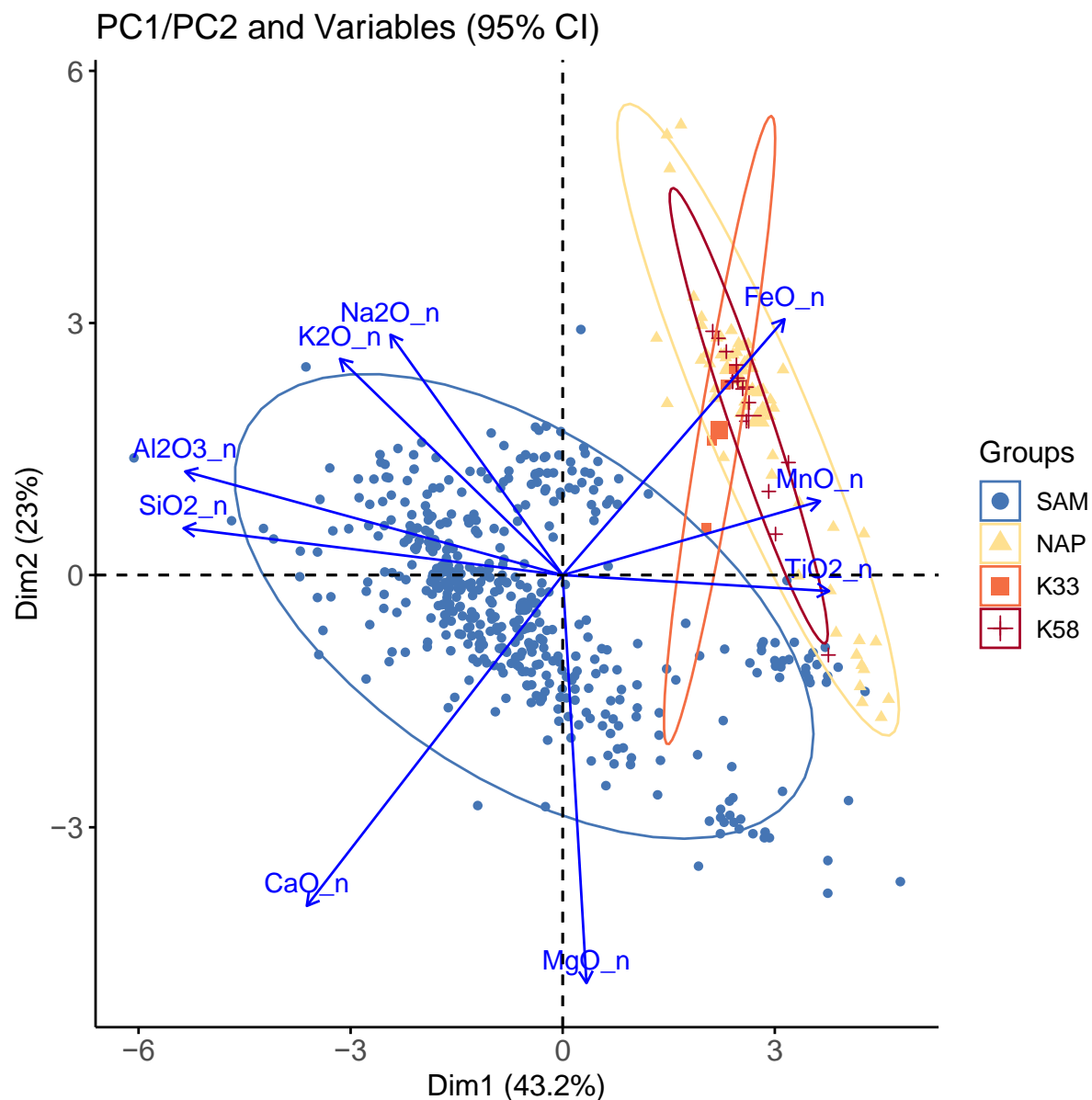
Figure S18. Principal components analysis showing the PC2 versus PC1 biplot, which explains >66% of the variance in the centred log ratio (clr) transformed major element EPMA dataset comprised of rhyolitic glass shard data from 33 cm (K33) and 58 cm (K58) depth in the Kiteschsee Lake record, and a database of published EPMA rhyolitic glass shard data from the Northern Antarctic Peninsula (NAP) and South America (Sam) (n = 545, rows with infinite values removed – see R code for details; datafile available in the Data Availability section). Data were plotted by group and filtered to remove totals <95%. There were insufficient rhyolitic shards from Deception Island (DI, n=2) in the database for PCA analysis.

Table S1 (overpage). (A) Chronological data for the Kiteschsee Lake record. Notes: OXCAL v. 4.4 using the SHCal20 Southern Hemisphere atmosphere dataset (Bronk Ramsey, 2001; Bronk Ramsey, 2009; Heaton et al., 2020). Absolute percentage of modern carbon (pMC) data were corrected according to 13C/12C isotopic ratios from measured pMC, where a "modern" pMC value is defined as 100% (1950 CE). Post-bomb (>1950 CE) samples were corrected according to $^{13}C/^{12}C$ isotopic ratios from measured pMC, where the 'present day' pMC value is defined as 107.5% (2010 CE) and calibrated using the SHCal13 SH Zone 1-2 Bomb curve in CALIBomb (Reimer and Reimer, 2004; Hua et al., 2013). As-measured and calibrated ages data are in regular type; correlation, modelled and reservoir corrected ages are in italics; tephra correlation ages from Yanou Lake (YAN) and Ardley Lake (ARD) with their equivalent depths in the KITE record are based on the tephra count data shown in Figures S4, S5; *=estimated ^{13}C isotope value due to insufficient material for IRMS analysis; red dash line indicates a possible hiatus; Laboratory ID prefixes B- were analysed by Beta Analytic, S-prefixes were analysed by SUERC. Calibrated ages are two-sigma (2σ; 95.4%) maximum to minimum age ranges and mean. Modelled age ranges and weighted mean values are based on 95% confidence ranges, generated by the BACON Bayesian age-depth Markov Chain Monte Carlo method (Blaauw, 2010; Blaauw and Christen, 2011; Trachsel and Telford, 2016). (B) Modelled ages of the Yanou Lake tephra layer ages updated to 2020 calibration curves (adapted from data in Roberts et al. (2017)); 95CI is 95% confidence interval.

A

ID No.	Core ID No.	Tephra	Laboratory ID. No.	Core ID_core depth [stratigraphic depth]	Kite Strat. Depth (cm)	Kite Unit	Material dated or modelled age	$\delta^{13}C$ (‰ ± 0.1)	Radiocarbon age (14C a BP)	SHCal20 Calibrated Ages (a cal BP) 2σ range	Mean ± 2σ
26	K1		B-501582	KITE2.1M_0–0.5 cm	0.25	10	AM: *Drepanocladus longifolius* sp.	-27.4	−100 ± 30	-5 – -7	-6 ± 2
27	K2		B-516809	KITE2.1M_4.5–5 cm	4.75		AM: *Drepanocladus longifolius* sp.	-29.3	−130 ± 30	-6 – -7	-7 ± 2
28	K3		B-516810	KITE2.1S_0.5–1 cm	5.5	9	Bulk sediment	-18.4	1,350 ± 30*	750 – 370	560 ± 180
29	K4		B-504801	KITE2.1S_4.5–5 cm	9.5	9	Bulk sediment	-23.9	1,600 ± 30*	1,010 – 600	800 ± 200
-	Y1a	T1a	S-18934	YAN-T1a [5.5 cm]	12	9	AM: *Drepanocladus longifolius* sp.	-25.0	910 ± 40	905 – 680	780 ± 120
30	K5		B-497408	KITE2.1S_16–17 cm	21.5	7	Bulk sediment (glaciogenic)	-32.6	9,380 ± 30*	10,130 – 9,660	9,900 ± 240
31	K6		B-501584	KITE1.1_7.5–8 cm	36.25	5	Bulk sediment	-18.0	1,860 ± 30	1,830 – 1,620	1,750 ± 100
-	Y3a	T3a	B-316287	YAN-T3a [20 cm]	42.5	-	AM: *Drepanocladus longifolius* sp.	-29.0	3,370 ± 30	3,690 – 3,450	3,550 ± 100
32	K7		B-501585	KITE1.1_17–18 cm	45.75	5	Bulk sediment	-17.7	3,350 ± 30	3,680 – 3,450	3,530 ± 100
-	Y5b	T5$_{min.}$	S-18935	YAN-T5 min. [32 cm]	58	-	AM: *Campylium polygamum* sp.	-25.0	4,270 ± 40	4,870 – 4,580	4,760 ± 160
-	Y5a	T5$_{max.}$	S-22310	YAN-T5 max. [190 cm]	64	-	AM: *Campylium polygamum* sp.	-31.9	4,890 ± 40	5,710 – 5,470	5,570 ± 120
-	Y6	T6	S-22311	YAN-T6 [202 cm]	64.5 / 72	-	AM: *Campylium polygamum* sp.	-26.5	5,051 ± 40	5,900 – 5,600	5,760 ± 160
-	A7	T7	-	ARD-T7 [333–339 cm]	72	-	Modelled age	-	-	7,570 – 7,285	7,430 ± 140
33	K8		B-498331	KITE1.1_45–46 cm	74	1	Bulk sediment	-18.0	6,410 ± 30	7,430 – 7,170	7,300 ± 120

B

Layer	Type	ID Methods	Core Section	Min. Depth (cm)	Max. Depth (cm)	Mid. Depth (cm)	Layer thickness (cm)	Lower 95CI age (cal. a BP)	Upper 95CI age (cal. a BP)	Median age (cal. a BP)	Mean age (cal. a BP)
T1b	Airfall Tephra	XRF-CS	YAN8A1	2.6	3.8	3.2	1.2	297	652	443	445
T1a	Airfall Tephra	Visible	YAN8A1	4.5	5.5	5	1	555	919	714	717
T2	Airfall Tephra	Visible	YAN8A1	11.8	12.5	12.15	0.7	1,694	2,118	1,912	1,911
T3c	Airfall Tephra	XRF-CS	YAN8A1	16	16.5	16.25	0.5	2,685	3,108	2,914	2,913
T3b	Airfall Tephra	XRF-CS	YAN8A1	18	19.5	18.75	1.5	3,075	3,615	3,322	3,327
T3a	Airfall Tephra	Visible	YAN8A1	20.5	21	20.75	0.5	3,474	3,809	3,625	3,632
T4	Airfall Tephra	Visible	YAN8A1	24.5	25.5	25	1	3,915	4,449	4,165	4,164
T5b-2	Reworked Tephra	Visible	YAN8A1	56	57	56.5	1	5,194	5,588	5,444	5,419
T5b-1	Reworked Tephra	Visible	YAN8A1	63	65	64	2	5,194	5,588	5,444	5,419
T5a	Reworked Tephra	Visible	YAN8A1	130	145	137.5	15	5,194	5,588	5,444	5,419
T5a	Airfall Tephra	Visible	YAN9B1	182	190	186	8	5,194	5,603	5,460	5,436
T6	Airfall Tephra	Visible	YAN9B1	202	205	203.5	3	5,630	6,051	5,805	5,813
T7b	Reworked Tephra	Visible	YAN9B1	226	226.5	226.25	0.5	6,048	6,658	6,344	6,345
T7a	Airfall Tephra	Visible	YAN8B1	248	259	253.5	11	6,598	7,239	6,915	6,916

Data input / Output [ka cal BP]	Artigas moraine Terrestrial Moss ages	Shetland-I Terrestrial Moss ages	Potter Peninsula - Terrestrial / Marine max. ages	BIC Foreland Moraines max. ages	KGI Advance max. ages	Readvance phase	KGI Retreat min. ages	Fildes lakes: basal ages	Fildes lakes: aquatic moss ages	Kaplan et al. (2020): JRI Advance ages	Kaplan et al. (2020): JRI Retreat ages
n	13	35	29	43	80		28	10	23	31	22
numMix	10	40	30	50	80		40	15	20	30	20
Probability	0.95	0.95	0.95	0.95	0.95		0.95	0.95	0.95	0.95	0.95
						4					
Phase 1	1.14 – 1.44	0.22 – 0.37	1.42 – 2.23	0.07 – 1.49	0.19 – 1.50	3	0.15 – 7.00	5.75 – 8.65	-0.01 – 0.97	0.05 – 0.53	2.73 – 4.25
Phase 2	1.69 – 2.05	0.42 – 0.89	6.99 – 8.23	1.67 – 2.24	1.68 – 2.47	2.4	1.12 – 2.03	9.21 – 10.02	1.03 – 1.53	1.18 – 2.17	4.37 – 5.93
Phase 3		0.92 – 1.38	9.29 – 10.06	2.59 – 3.00	2.51 – 2.98	2.3	4.90 – 8.60	10.39 – 11.11	1.88 – 2.44	2.61 – 3.07	7.17 – 11.05
Phase 4		1.67 – 2.20		3.13 – 3.49	3.30 – 3.87	2.2	9.44 – 10.10		3.33 – 3.83	3.22 – 5.91	11.46 – 12.26
Phase 5		2.59 – 3.06		5.27 – 6.32	4.52 – 4.75	2.1			4.28 – 5.25	6.16 – 7.73	
Phase 6		3.19 – 3.58		6.54 – 6.80	5.26 – 5.60				5.40 – 5.94	7.83 – 8.46	
Phase 7					5.64 – 6.31				6.17 – 6.66		
Phase 8					6.42 – 6.63	1			6.94 – 7.41		
Phase 9					7.31 – 8.02						
Phase 10					9.54 – 9.73						
Probability	0.68	0.68	0.68	0.68	0.68		0.68	0.68	0.68	0.68	0.68
Phase 1	1.79 – 1.98	0.56 – 0.65	7.28 – 7.83	0.51 – 0.78	0.63 – 0.72		1.31 – 1.77	5.87 – 7.22	-0.01 – 0.15	0.05 – 0.36	2.95 – 3.61
Phase 2		1.10 – 1.34		1.13 – 1.43	1.20 – 1.44		2.37 – 2.98	7.92 – 8.45	0.26 – 0.34	1.41 – 1.93	5.09 – 5.57
Phase 3		1.76 – 2.16		1.73 – 2.09	1.74 – 2.20		3.41 – 3.50	10.64 – 10.78	0.64 – 0.88	3.44 – 5.05	7.46 – 8.59
Phase 4		2.64 – 2.85		2.66 – 2.90	2.95 – 2.91		5.05 – 5.66		1.13 – 1.40	6.87 – 7.41	9.30 – 10.27
Phase 5				3.32 – 3.38	6.09 – 6.21		5.96 – 7.51		2.04 – 2.28		
Phase 6				5.35 – 5.46	7.36 – 7.91		7.93 – 8.09		3.50 – 3.61		
Phase 7				6.05 – 6.22					4.37 – 4.66		
Phase 8									4.79 – 5.09		
Phase 9									5.55 – 5.85		
Phase 10									7.21 – 7.27		

Table S2. Probability density phases constraining on the timing of glacier readvances on King George Island (KGI) at 95% and 68% probability. Phase analysis was also undertaken on minimum age constraints on the timing of glacier retreat for KGI, basal ages and aquatic moss layers from Fildes Peninsula lakes, and ages constraining readvances and retreat on the eastern Peninsula in Kaplan et al. (2020).

Environmental Variable	Time	Sr	Fe	Ca	K	Ti	Inc/Coh	Zn	Clay	Sand	Silt	Tephra counts/g
Eigen value	0.2054	0.0830	0.0602	0.0356	0.0643	0.0404	0.0591	0.0565	0.0445	0.0428	0.0387	0.0270
Explained variation	20.54	8.30	6.02	3.56	6.43	4.04	5.91	5.72	4.45	4.28	3.87	2.70
p value	0.002	0.024	0.088	0.374	0.068	0.286	0.128	0.096	0.4673	0.256	0.33	0.596

Table S3. Summary variance for geochemical, grain size and tephra variables (with p-value significance) in explaining diatom assemblage variations down-core. Significant variables (p<0.05) are highlighted in grey.

RDA axes	1	2	3	4
Eigenvalue	0.2670	0.7088	0.0369	0.0278
Explained variation (cumulative)	26.70	34.58	38.28	41.05
Pseudo-canonical correlation	0.8417	0.7980	0.6929	0.7682
Explained variance of species-env relationship	60.92	78.91	87.34	93.67

Table S4. Summary of output table from RDA using environmental variables (depth, inc./coh., TSC, Fe, Sr, Zn) to determine drivers of variation in diatom assemblages.

ID	LabID	SiO$_2$	TiO$_2$	Al2O$_3$	FeO	MnO	MgO	CaO	Na$_2$O	K$_2$O	P$_2$O$_5$	Total	Type	TAS Class
K33-1	RH0831	71.58	0.36	13.52	2.28	0.12	0.27	0.56	5.07	2.92	0.04	96.72	Acid	Rhyolite
K33-2	RH0831	50.28	1.92	14.89	9.75	0.16	6.08	9.59	4.13	0.55	0.29	97.62	Basic	Basalt
K33-3	RH0831	50.93	2.01	14.72	10.00	0.17	6.21	9.74	3.91	0.48	0.30	98.46	Basic	Basalt
K33-4	RH0831	56.14	2.21	15.37	9.40	0.17	3.17	6.49	5.29	0.90	0.39	99.54	Intermediate	Basaltic Trachyandesite
K33-5	RH0831	54.58	1.54	16.32	8.33	0.14	4.26	8.33	4.90	0.72	0.27	99.40	Intermediate	Basaltic Trachyandesite
K33-6	RH0831	69.71	-0.02	16.68	0.07	0.01	1.65	3.55	2.89	1.19	0.00	95.74	Acid	NC
K33-7	RH0831	53.55	1.55	16.68	8.58	0.13	4.56	8.64	4.58	0.59	0.25	99.11	Intermediate	Basaltic Andesite
K33-8	RH0831	57.33	2.12	15.04	8.83	0.17	2.83	5.74	4.60	1.06	0.46	98.19	Intermediate	Andesite
K33-9	RH0831	69.90	0.33	13.08	2.99	0.13	0.21	0.68	6.01	2.36	0.03	95.72	Acid	Rhyolite
K33-10	RH0831	55.50	1.51	16.72	7.38	0.14	4.02	7.70	4.95	0.71	0.25	98.88	Intermediate	Basaltic Andesite
K33-11	RH0831	55.31	1.57	16.81	7.69	0.14	4.15	7.84	4.93	0.66	0.27	99.37	Intermediate	Basaltic Andesite
K33-12	RH0831	64.65	0.64	14.56	5.20	0.17	0.59	2.20	6.18	1.76	0.16	96.11	Acid	Trachyte
K33-13	RH0831	52.06	2.68	14.67	11.76	0.20	4.32	8.10	4.39	0.61	0.31	99.09	Intermediate	Basaltic Andesite
K33-14	RH0831	54.20	1.52	16.67	8.22	0.15	4.54	8.74	5.02	0.64	0.24	99.95	Intermediate	Basaltic Trachyandesite
K33-15	RH0831	55.67	1.54	16.30	7.90	0.14	3.90	7.77	5.06	0.69	0.25	99.22	Intermediate	Basaltic Trachyandesite
K33-16	RH0831	54.50	1.59	16.81	7.75	0.14	4.16	8.23	4.52	0.69	0.27	98.67	Intermediate	Basaltic Andesite
K33-17	RH0831	55.36	1.50	16.36	7.53	0.14	4.60	8.38	4.46	0.69	0.24	99.26	Intermediate	Basaltic Andesite
K33-18	RH0831	57.33	1.39	17.69	7.64	0.12	3.30	7.29	4.76	0.69	0.25	100.46	Intermediate	Andesite
K33-19	RH0831	56.13	1.54	16.46	7.70	0.15	3.87	7.49	5.06	0.69	0.25	99.34	Intermediate	Basaltic Andesite
K33-20	RH0831	58.35	1.52	16.64	6.27	0.14	3.34	6.40	5.38	0.96	0.29	99.29	Intermediate	Trachyandesite
K33-21	RH0831	54.32	1.58	16.32	7.92	0.15	4.23	8.09	4.82	0.69	0.26	98.38	Intermediate	Basaltic Trachyandesite
K33-22	RH0831	70.68	0.33	12.74	3.19	0.13	0.20	0.65	6.17	2.29	0.03	96.42	Acid	Rhyolite
K33-23	RH0831	54.42	1.65	16.11	8.01	0.14	4.33	8.04	4.52	0.64	0.28	98.16	Intermediate	Basaltic Andesite
K33-24	RH0831	57.17	1.46	16.16	7.53	0.14	3.45	6.69	5.10	0.88	0.27	98.87	Intermediate	Trachyandesite
K33-25	RH0831	73.37	0.34	14.45	2.83	0.10	0.38	1.01	6.14	2.31	0.04	100.96	Acid	Rhyolite
K58-1	RH0832	70.40	0.37	13.48	2.96	0.13	0.23	0.65	6.53	2.50	0.05	97.30	Acid	Rhyolite
K58-2	RH0832	70.80	0.34	13.23	3.28	0.12	0.23	0.62	6.28	2.34	0.04	97.29	Acid	Rhyolite
K58-3	RH0832	73.18	0.37	13.60	3.43	0.13	0.26	0.71	6.69	2.46	0.05	100.88	Acid	Rhyolite
K58-4	RH0832	71.15	0.37	13.78	3.25	0.14	0.21	0.69	6.73	2.52	0.04	98.88	Acid	Rhyolite
K58-5	RH0832	71.58	0.38	13.72	3.12	0.14	0.22	0.73	6.69	2.47	0.05	99.08	Acid	Rhyolite
K58-6	RH0832	72.15	0.48	14.23	3.44	0.17	0.31	0.87	6.83	2.35	0.07	100.89	Acid	Rhyolite
K58-7	RH0832	71.34	0.36	13.69	3.03	0.13	0.18	0.65	6.45	2.66	0.04	98.54	Acid	Rhyolite
K58-8	RH0832	71.07	0.63	14.66	3.67	0.13	0.57	1.55	6.05	2.23	0.13	100.70	Acid	Rhyolite
K58-9	RH0832	71.32	0.36	13.74	3.18	0.14	0.26	0.66	6.81	2.51	0.05	99.03	Acid	Rhyolite
K58-10	RH0832	71.55	0.38	13.33	3.18	0.14	0.22	0.71	6.47	2.49	0.04	98.52	Acid	Rhyolite
K58-11	RH0832	71.50	0.38	13.63	3.19	0.13	0.27	0.73	6.63	2.28	0.05	98.80	Acid	Rhyolite
K58-12	RH0832	71.11	0.37	13.43	3.29	0.12	0.19	0.71	6.76	2.38	0.04	98.40	Acid	Rhyolite
K58-13	RH0832	71.76	0.36	13.62	3.16	0.13	0.17	0.71	6.83	2.44	0.03	99.20	Acid	Rhyolite
K58-14	RH0832	71.75	0.43	13.81	3.32	0.14	0.40	1.08	6.65	2.23	0.05	99.85	Acid	Rhyolite
K58-15	RH0832	71.25	0.36	13.74	3.19	0.14	0.23	0.69	6.60	2.45	0.04	98.70	Acid	Rhyolite
K58-16	RH0832	70.08	0.44	13.04	3.08	0.13	0.34	0.91	6.74	2.28	0.06	97.11	Acid	Rhyolite

Table S5. Electron probe microanalysis (EPMA) of glass shards (>95% total only) from the two most prominent tephra count peaks in the Kiteschsee Lake sediment record at 33 cm (KITE_33) and 58 cm (KITE_58) depth.

Group 1

[1]	NAP-18_PC079/2/149-9_UK_Deception	NAP-15_PC079/2/149-6_UK_Deception	NAP-17_PC079/2/149-8_UK_Deception	NAP-185_PC029/1/76-2_UK_Deception
[5]	NAP-55_GC027/2/4-8_UK_Deception	NAP-56_GC027/2/4-9_UK_Deception	NAP-14_PC079/2/149-5_UK_Deception	NAP-156_KC081/1/4-6_UK_Deception
[9]	NAP-153_KC081/1/4-3_UK_Deception	NAP-154_KC081/1/4-4_UK_Deception	NAP-224_PC029/1/80-23_UK_Deception	NAP-155_KC081/1/4-5_UK_Deception
[13]	NAP-1104_L6_228_T4_Deception	NAP-1153_BP_L6-A_86_T3_Deception	NAP-225_PC029/1/80-24_UK_Deception	NAP-1103_L6_230_T4_Deception
[17]	NAP-1154_BP_L6-A_86_T3_Deception	NAP-1102_L6_210_T4_Deception	NAP-1152_BP_L6-A_86_T3_Deception	NAP-184_PC029/1/76-1_UK_Deception
[21]	NAP-10_PC079/2/149-1_UK_Deception	NAP-12_PC079/2/149-3_UK_Deception	NAP-151_KC081/1/4-1_UK_Deception	NAP-53_GC027/2/4-6_UK_Deception
[25]	NAP-54_GC027/2/4-7_UK_Deception	NAP-51_GC027/2/4-4_UK_Deception	NAP-52_GC027/2/4-5_UK_Deception	NAP-48_GC027/2/4-1_UK_Deception
[29]	NAP-83_GC037/1/82-3_UK_Deception	NAP-13_PC079/2/149-4_UK_Deception	NAP-152_KC081/1/4-2_UK_Deception	NAP-202_PC029/1/80-1_UK_Deception
[33]	NAP-49_GC027/2/4-2_UK_Deception	NAP-50_GC027/2/4-3_UK_Deception	NAP-105_GC114/3/98-1_UK_Deception	NAP-11_PC079/2/149-2_UK_Deception
[37]	NAP-223_PC029/1/80-22_UK_Deception	K33-1_RH0831_UK_UK	NAP-186_PC029/1/76-3_UK_Deception	NAP-226_PC029/1/80-25_UK_Deception
[41]	K58-11_RH0832_UK_UK	NAP-410_YAN8B-1_41-41.5-14_T7b_Deception	K58-9_RH0832_UK_UK	NAP-444_PC460_73.5-74-22_T7a_Deception
[45]	K58-1_RH0832_UK_UK	K58-5_RH0832_UK_UK	K58-4_RH0832_UK_UK	K58-15_RH0832_UK_UK
[49]	NAP-16_PC079/2/149-7_UK_Deception	NAP-470_Beak1D_70.5-71-23_T10_Deception	K33-22_RH0831_UK_UK	K58-2_RH0832_UK_UK
[53]	K58-3_RH0832_UK_UK	K33-9_RH0831_UK_UK	K58-10_RH0832_UK_UK	NAP-472_Beak1D_70.5-71-25_T10_Deception
[57]	NAP-465_Beak1D_70.5-71-18_T10_Deception	NAP-458_Beak1D_70.5-71-11_T10_Deception	K58-7_RH0832_UK_UK	NAP-416_YAN8B-1_41-41.5-20_T7b_Deception
[61]	NAP-448_Beak1D_70.5-71-1_T10_Deception	NAP-421_YAN8B-1_41-41.5-25_T7b_Deception	K58-12_RH0832_UK_UK	K58-13_RH0832_UK_UK
[65]	NAP-82_GC037/1/82-2_UK_Deception	NAP-87_GC037/1/82-7_UK_Deception	NAP-85_GC037/1/82-5_UK_Deception	NAP-81_GC037/1/82-1_UK_Deception
[69]	NAP-88_GC037/1/82-8_UK_Deception			

Group 2

[1]	SAM-252_POLP1_90-94.5-14_UK_Solipuli	SAM-797_H2-Q_60-85_5_UK_Hudson	SAM-796_H2-Q_60-85_1_H2_Hudson	SAM-250_POLP1_90-94.5-12_UK_Solipuli
[5]	SAM-800_H2-Q_60-85_13_H2_Hudson	SAM-812_H2-E_0-30_11_H2_Hudson	SAM-175_POLP1_80-85-6_UK_Solipuli	SAM-260_POLP1_90-94.5-22_UK_Solipuli
[9]	SAM-806_H2-Q_60-85_28_H2_Hudson	SAM-196_POLP1_80-85-27_UK_Solipuli	SAM-255_POLP1_90-94.5-17_UK_Solipuli	SAM-189_POLP1_80-85-20_UK_Solipuli
[13]	SAM-258_POLP1_90-94.5-20_UK_Solipuli	SAM-801_H2-Q_60-85_14_H2_Hudson	SAM-818_H2-E_0-30_20_H2_Hudson	SAM-820_AVZ3-H2Q-60-85_4_H2_Hudson
[17]	SAM-821_AVZ3-H2Q-60-85_5_H2_Hudson	SAM-262_POLP1_90-94.5-24_UK_Solipuli	SAM-803_H2-Q_60-85_20_H2_Hudson	SAM-814_H2-E_0-30_16_H2_Hudson
[21]	SAM-180_POLP1_80-85-11_UK_Solipuli	SAM-256_POLP1_90-94.5-18_UK_Solipuli	SAM-802_H2-Q_60-85_18_H2_Hudson	SAM-816_H2-E_0-30_18_H2_Hudson
[25]	SAM-251_POLP1_90-94.5-13_UK_Solipuli	SAM-810_H2-E_0-30_7_H2_Hudson	SAM-176_POLP1_80-85-7_UK_Solipuli	SAM-809_H2-E_0-30_6_H2_Hudson
[29]	SAM-89_POR1_11-15-1_UK_Solipuli	SAM-823_AVZ3-H2Q-60-85_7_H2_Hudson	NAP-415_YAN8B-1_41-41.5-19_T7b_Deception	NAP-406_YAN8B-1_41-41.5-10_T7b_Deception
[33]	NAP-412_YAN8B-1_41-41.5-16_T7b_Deception	NAP-414_YAN8B-1_41-41.5-18_T7b_Deception	NAP-57_GC027/2/4-10_UK_Deception	K58-8_RH0832_UK_UK
[37]	NAP-60_GC027/2/4-13_UK_Deception	NAP-58_GC027/2/4-11_UK_Deception	NAP-157_KC081/1/4-7_UK_Deception	NAP-158_KC081/1/4-8_UK_Deception
[41]	NAP-187_PC029/1/76-4_UK_Deception	NAP-227_PC029/1/80-26_UK_Deception	NAP-205_PC029/1/80-4_UK_Deception	NAP-89_GC037/1/82-9_UK_Deception
[45]	NAP-84_GC037/1/82-4_UK_Deception	NAP-86_GC037/1/82-6_UK_Deception	K33-25_RH0831_UK_UK	K58-14_RH0832_UK_UK
[49]	K58-16_RH0832_UK_UK	NAP-463_Beak1D_70.5-71-16_T10_Deception	NAP-399_YAN8B-1_41-41.5-3_T7b_Deception	K58-6_RH0832_UK_UK

Group 3

[1]	SAM-355_COFL2_65-70-5_UK_Solipuli	SAM-353_COFL2_65-70-3_UK_Solipuli	SAM-351_COFL2_65-70-1_UK_Solipuli	SAM-356_COFL2_65-70-6_UK_Solipuli
[5]	SAM-365_COFL2_65-70-15_UK_Solipuli	SAM-375_COFR3_10-15-5_UK_Solipuli	SAM-358_COFL2_65-70-8_UK_Solipuli	SAM-241_POLP1_90-94.5-3_UK_Solipuli
[9]	SAM-387_COFR3_35-40-8_UK_Solipuli	SAM-242_POLP1_90-94.5-4_UK_Solipuli	SAM-368_COFL2_65-70-18_UK_Solipuli	SAM-379_COFR3_10-15-9_UK_Solipuli
[13]	SAM-364_COFL2_65-70-14_UK_Solipuli	SAM-377_COFR3_10-15-7_UK_Solipuli		

Table S6. Cluster groups 1–3 from analysis shown in Figure S17 containing K33 and K58 matches with NAP and South American (SAm) data. Group 3, and Groups 4–10 contain only South American matches.

Supplementary References

Antoniades D, Giralt S, Geyer A, Álvarez-Valero AM, Pla-Rabes S, Granados I, et al. (2018) The timing and widespread effects of the largest Holocene volcanic eruption in Antarctica. *Scientific Reports* 8: 17279.

Barnard A, Wellner JS and Anderson JB. (2014) Late Holocene climate change recorded in proxy records from a Bransfield Basin sediment core, Antarctic Peninsula. *Polar Research* 33.

Bentley MJ, Hodgson DA, Smith JA, Cofaigh CÓ, Domack EW, Larter RD, et al. (2009) Mechanisms of Holocene palaeoenvironmental change in the Antarctic Peninsula region. *The Holocene* 19: 51-69.

Bertler NAN, Mayewski PA and Carter L. (2011) Cold conditions in Antarctica during the Little Ice Age — Implications for abrupt climate change mechanisms. *Earth and Planetary Science Letters* 308: 41-51.

Binnie SA, Dunai TJ, Voronina E, Goral T, Heinze S and Dewald A. (2015) Separation of Be and Al for AMS using single-step column chromatography. *Nuclear Instruments and Methods in Physics Research Section B: Beam Interactions with Materials and Atoms* 361: 397-401.

Björck S, Håkansson H, Zale R, Karlén W and Jönsson BL. (1991a) A late Holocene lake sediment sequence from Livingston Island, South Shetland Islands, with palaeoclimatic implications. *Antarctic Science* 3: 61-72.

Björck S, Hjort, C., Ingolfsson, O., Skog, G. (1991b) Radiocarbon dates from the Antarctic Peninsula region — problems and potential. In: Lowe JJ (ed) *Radiocarbon dating: recent applications and future potential.* Quaternary Proceedings 1: 55–65.

Björck, S, Sandgren, P. and Zale, R. (1991c) Late Holocene tephrochronology of the northern Antarctic Peninsula. *Quaternary Research* 36(3): 322-328.

Björck S, Håkansson H, Olsson S, Barnekow L and Janssens J. (1993) Palaeoclimatic studies in South Shetland Islands, Antarctica, based on numerous stratigraphic variables in lake sediments. *Journal of Paleolimnology* 8: 233-272.

Björck S, Håkansson H, Olsson S, Ellis-Evans C, Humlum O and Lirio JM. (1996) Late Holocene palaeoclimatic records from lake sediments on James Ross Island, Antarctica. *Palaeogeography, Palaeoclimatology, Palaeoecology* 113: 195-220.

Blaauw M. (2010) Methods and code for 'classical' age-modelling of radiocarbon sequences. *Quaternary Geochronology* 5: 512-518.

Blaauw M and Christen JA. (2011) Flexible paleoclimate age-depth models using an autoregressive gamma process. *Bayesian Anal.* 6: 457-474.

Blaikie, J. (2020) Palaeoenvironmental reconstruction of Late Glacial-Holocene environmental change for Patagonia, southern South America. Unpublished PhD thesis, University of Stirling, http://hdl.handle.net/1893/31815.

Blockley, SPE, Pyne-O'Donnell, SDF., Lowe, JJ, Matthews, IP, Stone, A, Pollard, AM, Turney, CSM and Molyneux, EG. (2005) A new and less destructive laboratory procedure for the physical separation of distal glass tephra shards from sediments. *Quaternary Science Reviews* 24(16-17): 1952-1960.

Blott SJ and Pye K. (2001) GRADISTAT: A grain size distribution and statistics package for the analysis of unconsolidated sediments. *Earth Surface Processes and Landforms* 26: 1237-1248.

Bronk Ramsey C. (2001) Development of the Radiocarbon Calibration Program. *Radiocarbon* 43: 355-363.

Bronk Ramsey C. (2009) Bayesian Analysis of Radiocarbon Dates. *Radiocarbon* 51: 337-360.

Christ AJ, Talaia-Murray M, Elking N, Domack EW, Leventer A, Lavoie C, et al. (2015) Late Holocene glacial advance and ice shelf growth in Barilari Bay, Graham Land, west Antarctic Peninsula. *GSA Bulletin* 127: 297-315.

Clapperton CM and Sugden DE. (1988) Holocene Glacier Fluctuations in South-America and Antarctica. *Quaternary Science Reviews* 7: 185-198.

Davies SJ, Lamb HF and Roberts SJ. (2015) Micro-XRF Core Scanning in Palaeolimnology: Recent Developments. In: Croudace IW and Rothwell RG (eds) *Micro-XRF Studies of Sediment Cores: Applications of a non-destructive tool for the environmental sciences.* Dordrecht: Springer Netherlands, 189-226.

Dewald A, Heinze S, Jolie J, Zilges A, Dunai T, Rethemeyer J, et al. (2013) CologneAMS, a dedicated center for accelerator mass spectrometry in Germany. *Nuclear Instruments and Methods in Physics Research Section B: Beam Interactions with Materials and Atoms* 294: 18-23.

Domack EW, Ishman SE, Stein AB, McClennen CE and Jull AJT. (1995) Late Holocene Advance of the Muller Ice Shelf, Antarctic Peninsula - Sedimentological, Geochemical and Paleontological Evidence. *Antarctic Science* 7: 159-170.

Domack E, Leventer A, Dunbar R, Taylor F, Brachfeld S and Sjunneskog C. (2001) Chronology of the Palmer Deep site, Antarctic Peninsula: a Holocene palaeoenvironmental reference for the circum-Antarctic. *The Holocene* 11: 1-9.

Dunlea AG, Murray RW, Tada R, et al. (2020) Intercomparison of XRF Core Scanning Results From Seven Labs and Approaches to Practical Calibration. *Geochemistry, Geophysics, Geosystems* 21: e2020GC009248.

Esposito RMM, Spaulding SA, McKnight DM, Van de Vijver B, Kopalová K, Lubinski D, et al. (2008) Inland diatoms from the McMurdo Dry Valleys and James Ross Island, Antarctica. *Botany* 86: 1378-1392.

Forte P and Castro JM. (2019) H2O-content and temperature limit the explosive potential of rhyolite magma during Plinian eruptions. *Earth and Planetary Science Letters* 506: 157-167.

Foster LC, Pearson EJ, Juggins S, Hodgson DA, Saunders KM, Verleyen E, et al. (2016) Development of a regional glycerol dialkyl glycerol tetraether (GDGT)–temperature calibration for Antarctic and sub-Antarctic lakes. *Earth and Planetary Science Letters* 433: 370-379.

Fretzdorff S and Smellie JL. (2002) Electron microprobe characterization of ash layers in sediments from the central Bransfield basin (Antarctic Peninsula): evidence for at least two volcanic sources. *Antarctic Science* 14: 412-421.

Geyer A, Álvarez-Valero AM, Gisbert G, Aulinas M, Hernández-Barreña D, Lobo A, et al. (2019) Deciphering the evolution of Deception Island's magmatic system. *Scientific Reports* 9: 373.

Gibson JAE and Zale R. (2006) Holocene development of the fauna of Lake Boeckella, northern Antarctic Peninsula. *The Holocene* 16: 625-634.

Guglielmin M, Convey P, Malfasi F and Cannone N. (2015) Glacial fluctuations since the 'Medieval Warm Period' at Rothera Point (western Antarctic Peninsula). *The Holocene* 26: 154-158.

Hall BL. (2007) Late-Holocene advance of the Collins Ice Cap, King George Island, South Shetland Islands. *The Holocene* 17: 1253-1258.

Hall BL. (2010) Holocene relative sea-level changes and ice fluctuations in the South Shetland Islands. *Global and Planetary Change* 74: 15-26.

Hall BL, Henderson GM, Baroni C and Kellogg TB. (2010) Constant Holocene Southern-Ocean 14C reservoir ages and ice-shelf flow rates. *Earth and Planetary Science Letters* 296: 115-123.

Hass HC, Kuhn G, Monien P, Brumsack H-J and Forwick M. (2010) Climate fluctuations during the past two millennia as recorded in sediments from Maxwell Bay, South Shetland Islands, West Antarctica. *Geological Society, London, Special Publications* 344: 243-260.

Haworth EY. (1976) Two Late-Glacial (Late Devensian) Diatom Assemblage Profiles from Northern Scotland. *The New Phytologist* 77: 227-256.

Hayward, C. (2012) High spatial resolution electron probe microanalysis of tephras and melt inclusions without beam-induced chemical modification. *The Holocene* 22(1):119-125.

Heaton TJ, Köhler P, Butzin M, Bard E, Reimer RW, Austin WEN, et al. (2020) Marine20—The Marine Radiocarbon Age Calibration Curve (0–55,000 cal BP). *Radiocarbon* 62: 779-820.

Heroy DC, Sjunneskog C and Anderson JB. (2008) Holocene climate change in the Bransfield Basin, Antarctic Peninsula: evidence from sediment and diatom analysis. *Antarctic Science* 20: 69-87.

Hobbs WO, Telford RJ, Birks HJB, Saros JE, Hazewinkel RRO, Perren BB, et al. (2010) Quantifying Recent Ecological Changes in Remote Lakes of North America and Greenland Using Sediment Diatom Assemblages. *PLOS ONE* 5: e10026.

Hodgson, DA, Dyson, CL, Jones, VJ and Smellie, JL (1998) Tephra analysis of sediments from Midge Lake (South Shetland Islands) and Sombre Lake (South Orkney Islands), Antarctica. *Antarctic Science* 10(1): 13-20.

Hodgson DA, Roberts SJ, Smith JA, Verleyen E, Sterken M, Labarque M, et al. (2013) Late Quaternary environmental changes in Marguerite Bay, Antarctic Peninsula, inferred from lake sediments and raised beaches. *Quaternary Science Reviews* 68: 216-236.

Hogg AG, Heaton TJ, Hua Q, Palmer JG, Turney CSM, Southon J, et al. (2020) SHCal20 Southern Hemisphere Calibration, 0–55,000 Years cal BP. *Radiocarbon* 62: 759-778.

Hua Q, Barbetti M and Rakowski AZ. (2013) Atmospheric radiocarbon for the period 1950-2010. *Radiocarbon* 55: 1–14.

Janoušek, V, Farrow, CM and Erban, V. (2006) Interpretation of whole-rock geochemical data in igneous geochemistry: introducing Geochemical Data Toolkit (GCDkit). *Journal of Petrology* 47(6): 1255-1259.

Jones VJ and Juggins S. (1995) The construction of a diatom-based chlorophyll a transfer function and its application at three lakes on Signy Island (maritime Antarctic) subject to differing degrees of nutrient enrichment. *Freshwater Biology* 34: 433-445.

Juggins S. (2007) C2 Version 1.5 User Guide. Software for ecological and palaeoecological data analysis and visualisation. Newcastle University.

Juggins S. (2022) Rioja: Analysis of Quaternary Science Data, R package version (1.0-5).

Kaplan MR, Strelin JA, Schaefer JM, Peltier C, Martini MA, Flores E, et al. (2020) Holocene glacier behavior around the northern Antarctic Peninsula and possible causes. *Earth and Planetary Science Letters* 534: 116077.

Kylander ME, Ampel L, Wohlfarth B, et al. (2011) High-resolution X-ray fluorescence core scanning analysis of Les Echets (France) sedimentary sequence: new insights from chemical proxies. *Journal of Quaternary Science* 26: 109-117.

Le Bas MJ, Le Maitre RW, Streckeisen A & Zanettin B. (1986). A chemical classification of volcanic rocks based on the total alkali-silica diagram. *Journal of Petrology* 27: 745-750.

Lee, YI, Lim, HS, Yoon, HI and Tatur, A. (2007) Characteristics of tephra in Holocene lake sediments on King George Island, West Antarctica: implications for deglaciation and paleoenvironment. *Quaternary Science Reviews* 26(25-28): 3167-3178.

Leventer A, Domack EW, Ishman SE, Brachfeld S, McClennen CE and Manley P. (1996) Productivity cycles of 200-300 years in the Antarctic Peninsula region: Understanding linkages among the sun, atmosphere, oceans, sea ice, and biota. *Geological Society of America Bulletin* 108: 1626-1644.

Liu XD, Sun LG, Xie ZQ, Yin XB and Wang YH. (2005) A 1300-year record of penguin populations at Ardley Island in the Antarctic, as deduced from the geochemical data in the ornithogenic lake sediments. *Arctic Antarctic and Alpine Research* 37: 490-498.

Lotter AF, Birks HJB and Zolitschka B. (1995) Late-glacial pollen and diatom changes in response to two different environmental perturbations: volcanic eruption and Younger Dryas cooling. *Journal of Paleolimnology* 14: 23-47.

Maclennan, J, Jull, M., Mckenzie, D, Slater, L, and Grönvold, K. (2002). The link between volcanism and deglaciation in Iceland. *Geochemistry, Geophysics, Geosystems* 3, 1-25.

Mansilla, CA, McCulloch, RD, and Morello, F. (2016). Palaeoenvironmental change in Southern Patagonia during the Lateglacial and Holocene: Implications for forest refugia and climate reconstructions. *Palaeogeography Palaeoclimatology Palaeoecology*, 447, 1-11.

Mansilla, CA, McCulloch, RD, and Morello, F. (2018). The vulnerability of the Nothofagus forest-steppe ecotone to climate change: palaeoecological evidence from Tierra del Fuego (~53°S). *Palaeogeography Palaeoclimatology Palaeoecology*, 508: 59-70.

Martinez-Macchiavello J, Tatur A, Servant-Vildary S and Del Valle R. (1996) Holocene environmental change in a marine-estuarine-lacustrine sediment sequence, King George Island, South Shetland Islands. *Antarctic Science* 8(4): 313-322.

Mäusbacher R, Müller J and Schmidt R. (1989) Evolution of postglacial sedimentation in Antarctic lakes (King George Island). *Zeitschrift für Geomorphologie* 33: 219–234.

McConnell JR, Chellman NJ, Mulvaney R, Eckhardt S, Stohl A, Plunkett G, et al. (2021) Hemispheric black carbon increase after the 13th-century Māori arrival in New Zealand. *Nature* 598: 82-85.

McCulloch, RD, and Davies, SJ. (2001). Late-glacial and Holocene palaeoenvironmental change in the central Strait of Magellan, southern Patagonia. *Palaeogeography, Palaeoclimatology, Palaeoecology* 173: 143-173.

McCulloch, RD, Fogwill, CJ, Sugden, DE, Bentley, MJ, and Kubik, PW. (2005). Chronology of the last glaciation in central Strait of Magellan and Bahía Inútil, southernmost South America. *Geografiska Annaler*, 87A(2) 289-312.

McCulloch, RD, Figueroa, MJ, Mengoni Goñalons, G., Mansilla, CA, and Barclay, R. (2016). A Holocene record of environmental change from Río Zeballos, central Patagonia. *The Holocene*, 27(7):941-950.

McCulloch RD, Mansilla CA, Morello F, De Pol-Holz R, San Roman M, Tisdall E, Torres J. (2019). Late glacial and Holocene landscape change and rapid climate and coastal impacts in the Canal Beagle, southernmost Patagonia. *Journal of Quaternary Science* 34(8): 674-684.

McCulloch, RD, Blaikie, J, Jacob, B, Mansilla, CA, Morello, F, De Pol-Holz, R, San Román, M, Tisdall, E, Torres, J. (2020). Late glacial and Holocene climate variability, southernmost Patagonia. *Quaternary Science Reviews* 229: 106131.

McCulloch, RD, Mansilla, CA, Martin, F, Borrero, L, Staff, RA, Tisdall, EW. (2021). The nature and timing of landscape change at Cerro Benítez, Última Esperanza, southern Patagonia (52°S): New insights into the history of megafaunal extinctions and human occupation. *Quaternary International* 601: 116-129.

Michel TJ, Saros JE, Interlandi SJ and Wolfe AP. (2006) Resource requirements of four freshwater diatom taxa determined by in situ growth bioassays using natural populations from alpine lakes. *Hydrobiologia* 568: 235-243.

Milliken KT, Anderson JB, Wellner JS, Bohaty SM and Manley PL. (2009) High-resolution Holocene climate record from Maxwell Bay, South Shetland Islands, Antarctica. *Geological Society of America Bulletin* 121: 1711-1725.

Monien P, Schnetger B, Brumsack H-J, Hass HC and Kuhn G. (2011) A geochemical record of late Holocene palaeoenvironmental changes at King George Island (maritime Antarctica). *Antarctic Science* 23: 255-267.

Moreton SG and Smellie JL. (1998) Identification and correlation of distal tephra layers in deep-sea sediment cores, Scotia Sea, Antarctica. *Annals of Glaciology* 27: 285-289.

Morgan V and van Ommen TD. (1997) Seasonality in late-Holocene climate from ice-core records. *The Holocene* 7: 351-354.

Mosley-Thompson E, Thompson L, Grootes P and Gundestrup N. (1990) Little Ice Age (Neoglacial) Paleoenvironmental Conditions At Siple Station, Antarctica. *Annals of Glaciology* 14: 199-204.

Mulvaney R, Abram NJ, Hindmarsh RCA, Arrowsmith C, Fleet L, Triest J, et al. (2012) Recent Antarctic Peninsula warming relative to Holocene climate and ice-shelf history. *Nature* 489: 141-144.

Narcisi B, Petit JR, Delmonte B, Basile-Doelsch I and Maggi V. (2005) Characteristics and sources of tephra layers in the EPICA-Dome C ice record (East Antarctica): Implications for past atmospheric circulation and ice core stratigraphic correlations. *Earth and Planetary Science Letters* 239: 253-265.

Nishiizumi K, Imamura M, Caffee MW, Southon JR, Finkel RC and McAninch J. (2007) Absolute calibration of 10Be AMS standards. *Nuclear Instruments and Methods in Physics Research Section B: Beam Interactions with Materials and Atoms* 258: 403-413.

Ó Cofaigh C, Davies BJ, Livingstone SJ, Smith JA, Johnson JS, Hocking EP, et al. (2014) Reconstruction of ice-sheet changes in the Antarctic Peninsula since the Last Glacial Maximum. *Quaternary Science Reviews* 100: 87-110.

Oksanen J. (2014) Vegan: Community Ecology Package. R package version 2.3-0. http://cran.r-project.org/web/packages/vegan/index.html.

Oliva M, Antoniades D, Serrano E, Giralt S, Liu EJ, Granados I, et al. (2019) The deglaciation of Barton Peninsula (King George Island, South Shetland Islands, Antarctica) based on geomorphological evidence and lacustrine records. *Polar Record* 55: 177-188.

Oppedal, LT, van der Bilt, WG, Balascio, NL and Bakke, J. (2018) Patagonian ash on sub-Antarctic South Georgia: expanding the tephrostratigraphy of southern South America into the Atlantic sector of the Southern Ocean. *Journal of Quaternary Science* 33(5): 482-486.

Oppenheim DR and Ellis-Evans JC. (1989) Depth-related changes in benthic diatom assemblages of a maritime Antarctic lake. *Polar Biology* 9: 525-532.

Panaretos P, Albert PG, Thomas ZA, Turney CSM, Stern CR, Jones G, et al. (2021) Distal ash fall from the mid-Holocene eruption of Mount Hudson (H2) discovered in the Falkland Islands: New possibilities for Southern Hemisphere archive synchronisation. *Quaternary Science Reviews* 266: 107074.

Pearson EJ, Juggins S, Talbot HM, Weckström J, Rosén P, Ryves DB, et al. (2011) A lacustrine GDGT-temperature calibration from the Scandinavian Arctic to Antarctic: Renewed potential for the

application of GDGT-paleothermometry in lakes. *Geochimica et Cosmochimica Acta* 75: 6225-6238.

Praetorius, S, Mix, A, Jensen, B, Froese, D, Milne, G, Wolhowe, M, Addison, J, and Prahl, F (2016). Interaction between climate, volcanism, and isostatic rebound in Southeast Alaska during the last deglaciation. Earth and Planetary Science Letters 452, 79-89.

Reimer RW and Reimer PJ. (2004) *CALIBomb - calibration of post-bomb C-14 data*. Available at: www.calib.org.

Reynolds CS. (1984) *The Ecology of Freshwater Phytoplankton.,* New York: Cambridge University Press.

Roberts SJ, Sigurvinsson JR, Westgate JA and Sandhu A. (2007) Late Pliocene glaciation and landscape evolution of Vestfírðir, Northwest Iceland. *Quaternary Science Reviews* 26: 243-263.

Roberts SJ, Monien P, Foster LC, Loftfield J, Hocking EP, Schnetger B, et al. (2017) Past penguin colony responses to explosive volcanism on the Antarctic Peninsula. *Nature Communications* 8: 14914.

Roberts SJ, McCulloch RD, Emmings JF, Davies SJ, Van Nieuwenhuyze W, Sterken M, et al. (2022) Late Glacial and Holocene Palaeolake History of the Última Esperanza Region of Southern Patagonia. *Frontiers in Earth Science* 10. doi:10.3389/feart.2022.813396

Sagredo, E.A., Moreno, P.I., Villa-Martínez, R., Kaplan, M.R., Kubik, P.W., Stern, C.R. (2011). Fluctuations of the Última Esperanza ice lobe (52∘S), Chilean Patagonia, during the last glacial maximum and termination 1. *Geomorphology* 125: 92–108.

Satow C, Gudmundsson A, Gertisser R, Ramsey CB, Bazargan M, Pyle DM, et al. (2021) Eruptive activity of the Santorini Volcano controlled by sea-level rise and fall. *Nature Geoscience* 14: 586-592.

Saunders KM, Roberts SJ, Perren B, et al. (2018) Holocene dynamics of the Southern Hemisphere westerly winds and possible links to CO_2 outgassing. *Nature Geoscience* 11: 650-655.

Scaife RG, Long AJ, Monteath AJ, Hughes PDM, Bentley MJ and Stone P. (2019) The Falkland Islands' palaeoecological response to millennial-scale climate perturbations during the Pleistocene–Holocene transition: Implications for future vegetation stability in the Southern Ocean islands. *Journal of Quaternary Science* 34: 609-620.

Simms AR, Ivins ER, DeWitt R, Kouremenos P and Simkins LM. (2012) Timing of the most recent Neoglacial advance and retreat in the South Shetland Islands, Antarctic Peninsula: insights from raised beaches and Holocene uplift rates. *Quaternary Science Reviews* 47: 41-55.

Smellie, JL. (1999) The upper Cenozoic tephra record in the south polar region: a review. *Global and Planetary Change* 21(1-3): 51-70.

Smellie JL. (2001) Lithostratigraphy and volcanic evolution of Deception Island, South Shetland Islands. *Antarctic Science* 13: 188-209.

Smith RE, Smith VC, Fontijn K, Gebhardt AC, Wastegård S, Zolitschka B, et al. (2019) Refining the Late Quaternary tephrochronology for southern South America using the Laguna Potrok Aike sedimentary record. *Quaternary Science Reviews* 218: 137-156.

Spaulding SA, McKnight DM, Stoermer EF and Doran PT. (1997) Diatoms in sediments of perennially ice-covered Lake Hoare, and implications for interpreting lake history in the McMurdo Dry Valleys of Antarctica. *Journal of Paleolimnology* 17: 403-420.

Spaulding SA, Van de Vijver B, Hodgson DA, McKnight DM, Verleyen E and Stanish L. (2010) Diatoms as indicators of environmental change in Antarctic and subantarctic freshwaters. In: Stoermer EF and Smol JP (eds) *The Diatoms: Applications for the Environmental and Earth Sciences.* 2nd ed. Cambridge: Cambridge University Press, 267-284.

Sterken M, Verleyen E, Sabbe K, Terryn G, Charlet F, Bertrand S, et al. (2008) Late Quaternary climatic changes in southern Chile, as recorded in a diatom sequence of Lago Puyehue (40°40′ S). *Journal of Paleolimnology* 39: 219-235.

Sterken M, Roberts S, Hodgson D, Vyverman W, Balbo AL, Sabbe K, et al. (2012) Holocene glacial and climate history of Prince Gustav Channel, northeastern Antarctic Peninsula. *Quaternary Science Reviews* 31: 93-111.

Stern, C.R., Moreno, P.I., Henríquez, W.I., Villa-Martínez, R., Sagredo, E., Aravena, J.C., de Pol-Holz, R. (2016). Holocene tephrochronology around Cochrane (~47°S), southern Chile. *Andean Geology* 43: 1–19.

Stone J, Fifield K, Beer J, Vonmoos M, Obrist C, Grajcar M, et al. (2004) Co-precipitated silver–metal oxide aggregates for accelerator mass spectrometry of 10Be and 26Al. *Nuclear Instruments and Methods in Physics Research Section B: Beam Interactions with Materials and Atoms* 223-224: 272-277.

Tatur, A, Valle, R and Barczuk, A. (1999) Discussion on the uniform pattern of Holocene tephrochronology in South Shetland Islands, Antarctica. *Polish Polar Studies, Proceedings of XXVI Polar Symposium*: 303-321.

Telford RJ, Barker P, Metcalfe S and Newton A. (2004) Lacustrine responses to tephra deposition: examples from Mexico. *Quaternary Science Reviews* 23: 2337-2353.

Tibshirani R, Walther G and Hastie T. (2001) Estimating the number of clusters in a data set via the gap statistic. Journal of the Royal Statistical Society: Series B (Statistical Methodology) 63: 411-423.

ter Braak CJF and Smilauer P. (2002) *CANOCO reference manual and CanoDraw for Windows user's guide: software for canonical community ordination (version 4.5),* Ithaca, NY, USA: Microcomputer Power.

Trachsel M and Telford RJ. (2016) All age–depth models are wrong, but are getting better. *The Holocene* 27: 860-869.

Van de Vijver B. (2008) Pinnularia obaesa sp. Nov. And p. Australorabenhorstii sp. Nov., two new large pinnularia (sect. Distantes) from the Antarctic King George Island (South Shetland Islands). *Diatom Research* 23: 221-232.

Van de Vijver B and Beyens L. (1997) The epiphytic diatom flora of mosses from Stromness Bay area, South Georgia. *Polar Biology* 17(6): 492-501.

Van de Vijver B, Sterken M, Vyverman W, Mataloni G, Nedbalová L, Kopalová K, et al. (2010) Four new non-marine diatom taxa from the subantarctic and antarctic regions. *Diatom Research* 25: 431-443.

Van de Vijver B, Ector L and Cox EJ. (2012) Ultrastructure of Diatomella balfouriana with a discussion of septum-like structures in diatom genera. *Diatom Research* 27: 213-221.

van der Bilt WGM, Bakke J, Werner JP, Paasche Ø, Rosqvist G and Vatle SS. (2017) Late Holocene glacier reconstruction reveals retreat behind present limits and two-stage Little Ice Age on subantarctic South Georgia. *Journal of Quaternary Science* 32: 888-901.

Watcham EP, Bentley MJ, Hodgson DA, Roberts SJ, Fretwell PT, Lloyd JM, et al. (2011) A new Holocene relative sea level curve for the South Shetland Islands, Antarctica. *Quaternary Science Reviews* 30: 3152-3170.

Willmott V, Domack EW, Canals M and Brachfeld S. (2006) A high resolution relative paleointensity record from the Gerlache-Boyd paleo-ice stream region, northern Antarctic Peninsula. *Quaternary Research* 66: 1-11.

Xiao W, Frederichs T, Gersonde R, Kuhn G, Esper O and Zhang X. (2016) Constraining the dating of late Quaternary marine sediment records from the Scotia Sea (Southern Ocean). *Quaternary Geochronology* 31: 97-118.